ARTICLE OPEN

Check for updates

Neuron type-specific proteomics reveals distinct Shank3 proteoforms in iSPNs and dSPNs lead to striatal synaptopathy in *Shank3B*$^{-/-}$ mice

Yi-Zhi Wang[1,3], Tamara Perez-Rosello[2,3], Samuel N. Smukowski[1], D. James Surmeier[2] and Jeffrey N. Savas[1]✉

Combinatorial expression of postsynaptic proteins underlies synapse diversity within and between neuron types. Thus, characterization of neuron-type-specific postsynaptic proteomes is key to obtaining a deeper understanding of discrete synaptic properties and how selective dysfunction manifests in synaptopathies. To overcome the limitations associated with bulk measures of synaptic protein abundance, we developed a biotin proximity protein tagging probe to characterize neuron-type-specific postsynaptic proteomes in vivo. We found Shank3 protein isoforms are differentially expressed by direct and indirect pathway spiny projection neurons (dSPNs and iSPNs). Investigation of *Shank3B*$^{-/-}$ mice lacking exons 13–16 within the *Shank3* gene, reveal distinct Shank3 protein isoform expression in iSPNs and dSPNs. In *Shank3B*$^{-/-}$ striatum, Shank3E and Shank3NT are expressed by dSPNs but are undetectable in iSPNs. Proteomic analysis indicates significant and selective alterations in the postsynaptic proteome of *Shank3B*$^{-/-}$ iSPNs. Correspondingly, the deletion of exons 13–16 diminishes dendritic spine density, reduces spine head diameter, and hampers corticostriatal synaptic transmission in iSPNs. Remarkably, reintroducing Shank3E in adult *Shank3B*$^{-/-}$ iSPNs significantly rectifies the observed dendritic spine morphological and corticostriatal synaptic transmission deficits. We report unexpected cell-type specific synaptic protein isoform expression which could play a key causal role in specifying synapse diversity and selective synapse dysfunction in synaptopathies.

Molecular Psychiatry; https://doi.org/10.1038/s41380-024-02493-w

INTRODUCTION

Postsynaptic specializations are essential for receiving and processing synaptic signals. The composition of postsynaptic proteomes varies from one brain region to the next, reflecting functional diversity [1–4]. This diversity is likely to extend to different cell types within brain regions. The striatum is a large subcortical structure involved in goal-directed actions and habits [5, 6]. The principal neurons of the striatum are GABAergic spiny projection neurons (SPNs). SPNs can be divided into direct and indirect pathway SPNs (dSPNs and iSPNs, respectively) on the basis of their axonal projections, expression of G-protein coupled receptors, and expression of releasable peptides [5–7]. The extra-striatal innervation of SPNs in the dorsal striatum is derived primarily from glutamatergic neurons in the cerebral cortex and thalamus, which form axospinous synapses. In addition, SPNs are innervated by other SPNs and by GABAergic and cholinergic interneurons [5–7].

Striatal dysfunction plays a major role in numerous neurodevelopmental and degenerative diseases such as Huntington's disease (HD) [8], Parkinson's disease (PD) [9] and autism spectrum disorder (ASD) [10]. Moreover, in each of these disorders, SPN-specific alterations in synaptic function play an important role in the emergence of symptoms [11–13]. However, the molecular basis of these cell-type specific synaptic changes remains largely unknown since traditional bulk protein methods lack cellular resolution [14].

MATERIALS AND METHODS

All materials used in this study are available upon request.

Animals

All procedures were approved by Northwestern University's Animal Care and Use Committee (IS00001789, IS00010673, IS00009321) in compliance with US National Institutes of Health standards. *Shank3B*$^{-/-}$ mice (B6.129-Shank3tm2Gfng/J, Stock No: 017688) were acquired from The Jackson Laboratory. We acquired frozen sperm of Drd1-Cre mouse (EY262Gsat/Mmucd, GENSAT Project, backcrossed to C57BL/6 J background, MMRRC ID, 17264) from Mutant Mouse Resource & Research Centers and bred Drd1-Cre mice with the help from Northwestern university Center for Comparative Medicine. Adora2-Cre mice, KG139Gsat/Mmucd, GENSAT Project, backcrossed to C57BL/6 J background, MMRRC ID, 36158. D2-EGFP (STOCK Tg(Drd2-EGFP)S118Gsat/Mmnc; GENSAT Project, backcrossed to C57BL/6 J background).

We first crossed homozygous Drd1-Cre, Adora2-Cre or D2-EGFP mice with *Shank3B*$^{-/+}$ mice to achieve Drd1-Cre$^{-/+}$::*Shank3B*$^{-/+}$, Adora2-Cre$^{-/+}$::*Shank3B*$^{-/+}$ and D2-EGFP$^{-/+}$::*Shank3B*$^{-/+}$ mice. Then we bred Drd1-Cre$^{+/+}$::*Shank3B*$^{-/+}$, Adora2-Cre$^{+/+}$::*Shank3B*$^{-/+}$ and D2 EGFP$^{+/+}$::*Shank3B*$^{-/+}$ mice to obtain Drd1-Cre::*Shank3B*$^{+/+}$, Drd1-Cre::*Shank3B*$^{-/-}$, Adora2-Cre::*Shank3B*$^{+/+}$, Adora2-Cre::*Shank3B*$^{-/-}$, D2-EGFP::*Shank3B*$^{+/+}$ and D2-EGFP::*Shank3B*$^{-/-}$ mice.

[1]Department of Neurology, Feinberg School of Medicine, Northwestern University, Chicago, IL 60611, USA. [2]Department of Neuroscience, Feinberg School of Medicine, Northwestern University, Chicago, IL 60611, USA. [3]These authors contributed equally: Yi-Zhi Wang, Tamara Perez-Rosello. ✉email: jeffrey.savas@northwestern.edu

Received: 22 March 2022 Revised: 16 February 2024 Accepted: 22 February 2024
Published online: 14 March 2024

For electrophysiological experiments examining the impact of our probes on synaptic transmission, 4-5-month-old Adora2-Cre mice were used. For all TMT-MS experiments, dendritic spine morphological analysis and electrophysiological experiments using D2-EGFP::*Shank3B*$^{+/+}$ and D2-EGFP::*Shank3B*$^{-/-}$ mice, eight-week old mice were used for intracranial AAV injections. For 10-plex TMT-MS experiments compared postsynaptic compartment proteomes of *Shank3B*$^{+/+}$ and *Shank3B*$^{-/-}$ SPNs used littermate controls. For AAV-based rescue experiments, ~three-month-old mice were used for intracranial AAV injections. For biochemical and IHC experiments, 8–12 weeks old mice were used. For biochemical, IHC, 3-plex TMT-MS and electrophysiological experiments, mice were randomly selected. Both male and female mice were used for all experiments.

Cloning

Our probes were based on BirA*-based proximity biotin-tagging [15] and the synaptic localization motifs from mGRASP [16]. We obtained pcDNA3.1 MCS-BirA(R118G)-HA, paavCAG-pre-mGRASP-mCerulean and paavCAG-post-mGRASP-2A-dTomato from Addgene (Cat#, 53581, 34910 and 34912, RRID: Addgene_53581, Addgene_34910 and Addgene_34912). Overlap extension PCR was used to construct BirA* probes. For postBirA*, we individually amplified SP, BirA*-HA, tr-mNL1 and 2A-GFP fragments by PCR. Then we constructed SP-BirA*-HA and tr-mNL1-2A-GFP by linking corresponding fragments using overlap extension PCR. These two fragments were digested by EcoRI (New England Biolabs, Cat# R0101) and then linked together using T4 DNA ligase (New England Biolabs, Cat# M0202) to form postBirA*. Then postBirA* fragment and pAAV-FLEX-GFP vector (Addgene, Cat# 28304) were both digested with KpnI (New England Biolabs, Cat# R3142) and BsrgI (New England Biolabs, Cat# R0575). FLEX-postBirA* was formed by linking digested postBirA* fragment with linearized pAAV-FLEX-GFP vector. Thus, the GFP coding sequence was replaced to postBirA*. FLEX-cytoBirA* and FLEX-preBirA* were constructed in a similar way. Mouse Shank3A and 3E plasmids were generously provided by Dr. Yong-Hui Jiang (Yale School of Medicine). Shank3NT was subcloned from the Shank3A expression construct. FLEX-Shank3E1, and FLEX-Shank3NT were similarly assembled into the pAAV-FLEX-GFP vector using the method described above.

Stereotaxic delivery of AAVs

Adora2-Cre::*Shank3B*$^{+/+}$, Adora2-Cre::*Shank3B*$^{-/-}$, Drd1-Cre::*Shank3B*$^{+/+}$ or Drd1-Cre::*Shank3B*$^{-/-}$ mice were anesthetized with isoflurane (Covertrus, Cat# 029405) before being placed in a stereotaxic injection rig (KOPF, model 922). Mouse head was restrained by ear bars with placing the front teeth in the holding apparatus. Isoflurane and oxygen were provided (Kent, VetFlo) at a low flow rate to keep the mouse anesthetized during the whole procedure. The animal's body temperature was maintained at 37–38 °C with an electric heating pad (Homeothermic blanket system, Harvard Apparatus). To prevent from drying, the eyeballs were covered with ophthalmic ointment (Artificial tears, Henry Schein). Buprenex (0.1 mg/kg) was administrated by intraperitoneal (IP) injection. AAVs were injected at two positions in each striatum using Hamilton needles (Hamilton, 65460-02). Injection sites, ±2.4 mediolateral, 0.5 anteroposterior, −3.0 and −3.5 dorsoventral. An automatic injection pump (World Precision Instruments) was used to control the speed at 200 nl/min. The needle was holding at injection position for 5 min before slow withdrawal. After closing the wound by wound clips, meloxicam (1 mg/kg) was administrated by IP injection. The mouse was put onto a warming pad for recovery. The next morning, meloxicam was administrated one more time to the AVV-infected mouse. One month later, biotin (24 mg/kg in saline) was administrated by subcutaneous (SubQ) injection for seven consecutive days [17]. For the no-biotin control experiments, saline was administrated by SubQ injection for seven consecutive days. Mice designated for dendritic spine morphological analysis were euthanized one-month post-AAV injection, without receiving any subcutaneous injections.

Electrophysiology and data analysis

The brains were rapidly removed and cooled in ice-cold oxygenated sucrose-Artificial cerebrospinal fluid (ACSF), comprised of (in mM) for GPe slices; sucrose 220; KCl 2.5; $CaCl_2$ 0.5, $MgSO_4$ 3, NaH_2PO_4 1.2, $NaHCO_3$ 26, glucose 5 and for striatal slices; NaCl 124; KCl 3; $CaCl_2$ 0.5, $NaH2PO_4$ 1, $NaHCO_3$ 26, glucose 5. Coronal (275 µm) band para-sagittal slices (300 µm) were prepared in ice-cold oxygenated (95% O_2 / 5% CO_2) ACSF with a vibratome (LeicaVT1000S, Leica Biosystems, Germany), then warmed to 36 °C for 30 to 45 min, allowed to cool to room temperature, and transferred as needed to a submerged slice chamber mounted on the stage of an upright microscope, perfused at 2 ml/min with oxygenated normal ACSF, comprised of (in mM): NaCl 124; KCl 3.5, $CaCl_2$ 2.5, $MgSO_4$ 1.2, NaH_2PO_4 1.2, $NaHCO_3$ 26, glucose 11. Cell attach and whole-cell patch clamp recordings in voltage clamp mode were made using a MultiClamp 700B amplifier (Molecular Devices, California, Sunnyvale, USA). Recordings were performed with patch pipettes (3–5 MΩ resistance) containing (in mM): 126 $CsCH_3SO_3$, 8 NaCl, 10 HEPES, 2.9 QX-314, 8 Na_2-Phosphocreatine, 0.3 Na_2GTP, 4 MgATP, 0.1 $CaCl_2$, 1 EGTA (pH 7.2–7.3), and osmolarity adjusted to 285–290 mOsm. For the control experiments with the synaptic probes, we use a different solution (in mM) K-gluconate 145, EGTA 1.1, HEPES 10, $CaCl_2$ 0.1, $MgCl_2$ 4, Na_2ATP 2, NaGTP 0.3, pH adjusted to 7.2 EPSCs were recorded from indirect pathway spiny projection neurons (iSPNs) in voltage-clamp mode at a holding potential of -80 mV. Optogenetic methods were used to activate corticostriatal glutamatergic axons while simultaneously performing patch-clamp recordings from SPNs in the DLS. For the comparison of EPSCs peak amplitudes between D2-EGFP::*Shank3B*$^{+/+}$ and D2-EGFP::*Shank3B*$^{-/-}$ mice most of the EPSCs recorded from GFP positive (iSPNs) and GFP negative spiny neurons (dSPN) were made from the same slice. IPSCs were recorded from globus pallidus (GP) neurons in voltage-clamp mode at a holding potential of -40 mV. Evoked responses for input-output curves were averaged from $n = 3$ per stimulus intensity. Both input-output curves were derived from the peaks of the evoked currents.

Stereotaxic injections: Stereotaxic injections were performed using a computer-assisted stereotaxic system (Leica Biosystems, Buffalo Grove, IL). Mice were anesthetized with isoflurane. The injection coordinates were: for striatal injections of FLEX-cytoBirA*, FLEX-preBirA*, and pAAV-EF1a-double floxed-hChR2(H134R)-mCherry-WPRE-HGHpA (lateral, 2.70 mm; posterior, -0.10 mm; depth, 3.40 mm); for dorso lateral striatum (DLS) injections of FLEX-cytoBirA*, FLEX-postBirA* and FLEX-Shank3E1 AAVs (lateral, 2.15 mm; posterior, 1.18 mm; depth, 1.33 mm), and for the cortical injections of pAAV-hSyn-hChR2(H134R)-mCherry (lateral, 1.51 mm; posterior, 0.98 mm; depth, 3.40 mm). In most of the experiments, the AAV-containing solution was injected at a moderate speed (2–3 psi) but in some of the experiments to maximize the extent of the infection the AAV-containing solution was injected at higher speed (4–6 psi) (IM 300 Microinjector, Narishige, Japan). Experiments with Cre-on construct were performed 4 weeks after injection whereas experiments with a ChR2 Cre-independent construct were performed two weeks after virus injection. The rescue experiments were performed 6 weeks after the infection with FLEX-Shank3E AAV.

Imaging: Slices were mounted with Vectashield (Vector, USA) and view under a laser scanning confocal microscope (FV 10i, Olympus). Images processing was done in Imaris (Bitplane, Zurich, Switzerland) and adjusted for contrast and brightness in Adobe Photoshop CC (Adobe Systems).

Data analysis. Evoked EPSCs and IPSCs were analyzed with pClamp 10 (Molecular Devices, California, Sunnyvale, USA) program. Statistical analysis was performed using GraphPad Prism 6.07 (GraphPad Software, Inc., La Jolla, CA, USA) and included either a one-way or a two-way ordinary ANOVA, followed by Bonferroni's multiple or comparisons test. Data are presented as mean ± SEM.

Immunohistochemistry (IHC) staining

Para-sagittal brain slices (200 µm) were prepared as descried above. Slices were briefly fixed in 4% paraformaldehyde (PFA, VWR, Cat# AA-A11313-36) in phosphate buffered saline (PBS, pH 7.4) for 15 min with mild agitation at room temperature and then washed 3 × 5 min in glycine solution (1 M glycine in PBS, pH 7.4) to block unreacted PFA. Slices were further washed 3 × 5 min in PBS to remove glycine. For permeabilization, slices were incubated in Triton X-100 (0.5% in PBS, pH7.4) solution for 1 hr. After blocking (10% horse serum, 0.5% Trition X-100 in PBS, pH7.4) for 1 hr, slides were incubated with primary antibodies at 4 °C for 48 h with mild agitation. Following primary antibodies were used: goat anti-BirA (1:200, MyBioSource, Cat# MBS534316, RRID:AB_10578606), chicken anti-GFP (1:1000, Abcam, Cat # ab13970, RRID:AB_300798), guinea pig anti-vGluT1 (1:1000, Millipore Sigma, Cat# AB5905, RRID:AB_2301751), rabbit anti-Gephyrin (1:500, Synaptic System, Cat# 147008, RRID:AB_2619834), mouse anti-PSD95 (1:400, Thermo Fisher Scientific, Cat# MA1-046, RRID:AB_2092361), rabbit anti-vGAT (1:500, Synaptic System, Cat #131003, RRID:AB_887869) and rabbit anti-Prkaca (1:500, Millipore Sigma, Cat# HPA071185, RRID:AB_2686356). After 6 ×5 min washing in PBS, slides were incubated with corresponding Alexa Fluor secondary antibodies (1:1000, Thermo Scientific, Cat#, A11030, A11057, A21057, A31571, A31573 and SA5-10098. RRID:

AB_2534089, AB_2534104, AB_2535723, AB_162542, AB_2536183 and AB_2556678) or NeutrAvidin-Rhoaminne Red (1:2000, Thermo Fisher Scientific, Cat# 6378) overnight at 4 °C with mild agitation. Then, after 3 × 5 min washing in PBS, slides were incubated in 4′,6-diamidino-2-phenylindole (1:1000, DAPI, Sigma-Aldrich, Cat# D9542) solution for 10 min. The slides were washed 3 × 5 min and mounted with Fluoromount-G (SouthernBiotech, Cat# 0100-01) on microscope slides with Secure-Seal spacer (Invitrogen, Cat# S24736).

For IHC experiments to detect Prkaca expression in iSPNs and dSPNs, Drd1-Cre or A2a-Cre mice were anesthetized and transcardially perfused with ice old PBS followed by 4% PFA. Dissected brains were cryoprotected in 30% sucrose solution and then buried in embedding medium (Sakura, Cat# 4583). Coronal sections (35 μm) were obtained using a cryostat microtome. IHC staining procedure was the same as staining 200 μm thick brain slices. Rabbit anti-Prkaca (1:400, Millipore Sigma, Cat# HPA071185) was used to probe Prkaca expressions in SPNs.

Wole brain slice images were captured using TissueGnostics with 20× objective lens. Images of synaptic proteins were captured using a Nikon A1R+ confocal laser microscope and 60× or 100× objective lens. For each mouse, brain slices were randomly selected. Images were processed and analyzed by Fiji (NIH) with plugins Ratioplus, Colocalization Finder, and JACOP.

Dendritic spine morphological analysis

Adora2-Cre::*Shank3B*$^{+/+}$, Adora2-Cre::*Shank3B*$^{-/-}$, Drd1-Cre::*Shank3B*$^{+/+}$ or Drd1-Cre::*Shank3B*$^{-/-}$ mice were intracranially injected with designated AAVs into striatum. One-month post-AAV injection, mice were euthanized and transcardially perfused as described above. Coronal sections (35 μm) were obtained using a cryostat microtome. Chicken anti-GFP (1:5000, Abcam, Cat # ab13970, RRID:AB_300798) and goat anti-chicken IgY (H + L) secondary antibody (1:2000, Alexa Fluor 488, Fisher Scientific, Cat# A11039) were used to enhance GFP signaling. IHC staining procedure was the same as described above. The slides were mounted with ProLong™ Diamond Antifade Mountant (Thermo Fisher Scientific, Cat# P36970).

Images were captured using a Nikon A1R+ confocal laser microscope and 60× objective lens in z-stack mode (the step was automatically optimized, 0.125 μm). For each mouse, brain slices were randomly selected. Only dendritic spines on secondary dendrites were analyzed. Spine density, spine head size and spine classification were analyzed with Imaris 10.0.0 (Oxford Instruments) based on a previously study [18]. The rules for spine classification: (1) Mushroom spines: dendritic protrusions with a head wider than 0.5 μm or twice the neck's width; (2) Stubby spines: short dendritic protrusions, up to 0.5 μm long, with an indistinct head; and (3) Thin/filopodia spines are long, slender dendritic extensions over 0.5 μm with a head narrower than 0.5 μm or without a distinct head.

Immunogold staining and silver enhancement

Para-sagittal brain slices (200 μm) were prepared as descried above. Slices were incubated with 4% PFA and 0.2% glutaraldehyde (Polysciences, Cat # BLI1909-10) in PBS (Corning, Cat #, 21-040-CV) for 15 min followed by two washes with 0.1% $NaBH_4$ (Sigma-Aldrich, Cat # 480886) in PBS (15 min each). Then slices were washed by 3 ×15 min with PBS and permeabilized with 0.005% Triton-X-100 (Sigma-Aldrich, Cat # X100) in PBS for one hours. Slices were incubated with Aurion blocking solution for one hour and washed 2 × 15 min with incubation solution (Electron microscopy sciences, Cat # 25558). Then the slices were incubated with goat anti-BirA in incubation solution (1:50, MyBioSource, Cat # MBS534316, RRID:AB_10578606) at 4 °C for 48 h with mild agitation. After 6 × 10 min washed with incubation solution, sliced were incubated with donkey-anti-goat UltraSmall gold (1:50, Electron microscopy sciences, Cat #25800, RRID:AB_2631210) at 4 °C for 24 h with mild agitation. Then slides were washed 6 ×10 min with incubation solution and followed by 2 ×10 min washes with PBS. Slices were post-fixed with 0.2% glutaraldehyde in PBS for 15 min and washed 4 ×10 min with MilliQ water. Slices were silver-enhanced with AURION R-GENT SE-EM kit (Electron microscopy sciences, Cat # 500.033) for 25 min. Then slices were washed 3 ×10 min in MilliQ water and sent to the Northwestern University Center for Advanced Microscopy for further processing. Briefly, samples were fixed in mixture of 2.5% glutaraldehyde and 2% paraformaldehyde in 0.1 M cacodylate buffer for 2 or 3 h or overnight at 4 °C. After post-fixation in 1% osmium tetroxide and 3% uranyl acetate cells were dehydrated in series of ethanol, embedded in Epon resin and polymerized for 48 h at 60 °C. Then ultrathin sections were made using Ultracut UC7 Ultramicrotome (Leica Microsystems) and contrasted with 3% uranyl acetate and Reynolds's lead citrate. Samples were imaged using a FEI Tecnai Spirit G2 transmission electron microscope (FEI Company, Hillsboro, OR) operated at 80 kV. Images were captured by Eagle 4k HR 200 kV CCD camera. Images were processed and analyzed by Fiji (NIH).

Affinity purification of biotinylated proteins

Mice were euthanized, and their brains were extracted. The striatum was then dissected using an adult mouse brain slicer matrix (Zivic Instruments, Cat# BSMAS005-1). Dissected striata were homogenized in RIPA lysis buffer (50 mM Tris, 150 mM NaCl, 0.1% SDS, 1 mM EDTA, 0.5% sodium deoxycholate, 1% Triton X-100, 1 x protease inhibitor cocktail (Thermo Fisher Scientific, Cat # 78443), 1 x phosphatase inhibitor (Thermo Fisher Scientific, Cat # 78420), pH 7.4) with an electronic homogenizer (Glas-Col, Cat # 099C-K54). Then excess 10% SDS solution was added into each sample to make the final SDS concentration to 1%. After sonication with a probe sonicator (Qsonica) for 3 ×1 min, striatal homogenates were solubilized at 4 °C for one hr with rotation. Insoluble components were removed by centrifuging at 13,000 × *g* for 30 min. 400 μl of pre-washed NeutrAvidin beads (Thermo Fisher Scientific, Cat # 2901) were added into each sample and incubated at 4 °C overnight with gentle rotation.

For silver staining, Coomassie blue (CBB) staining and Western blotting (WB), after overnight incubation with striatal homogenates, NeutrAvidin beads were rinsed for 5 × 5 min in 1 ml RIPA lysis buffer. Then 400 μl 2 x loading buffer were added into the beads. Mixtures were boiled at 95 °C for 5 min and immediately put onto ice to elute the biotinylated proteins from the beads. Supernatants were carefully collected and reduced to ~60 μl using a SpeedVac Vacuum Concentrator. Then all samples were brought up to 120 μl with RIPA lysis buffer. For silver staining, 20 μl of each sample was loaded into 4–12% Bis-Tris gels (Thermo Fisher, Cat # np0335box) for electrophoresis. For CBB staining and WB, 4–12% Tris-glycine gels (Invitrogen, Cat # XP04120BOX) were used.

Silver and CBB staining

We used Pierce Silver Stain Kit (Thermo Fisher, Cat# 24612) for silver staining. Gels were washed 2 × 5 min in ultrapure water and then fixed with 2 × 15 min in 30% ethanol: 10% acetic acid solution. Then the fixed gels were washed 2 × 5 min with 10% ethanol and 2 × 5 min in ultrapure water. Then the gels were sensitized for 1 min and washed twice 2 × 1 min with water. Then, the gels were stained for 30 min and washed 2 × 20 secs with ultrapure water. The gels were developed for 1–3 min until bands appear and stopped with 5% acetic acid for 10 min.

We used SimplyBlue™ SafeStain kit (Novex, Cat# LC6065) for CBB staining. Gels were washed 3 × 5 min in ultrapure water and stained with SimplyBlue™ SafeStain solution overnight at room temperature (RT) with mild agitation. The gels were washed for 2 ×1 hour in MiiliQ water to reduce background staining.

Western blotting (WB) and Streptavidin-horseradish peroxidase (HRP) blotting

After electrophoresis, proteins were transferred onto nitrocellulose membranes (Thermo Fisher, Cat# 4500002). For WB, the membranes were blocked with 10% bovine serum albumin (BSA, Jackson immunoResearch laboratories, Cat# 001-000-162) in TBST solution (Tris-buffered saline, 0.1% Tween 20) for one hour in RT. Then membranes were incubated with primary antibodies in incubation solution (3% BSA in TBST) overnight at 4 °C with mild agitation. Following primary antibodies were used: mouse anti-HA (1:1000, BioLegend, Cat# 901502, RRID:AB_2565007), chicken anti-GFP (1:2000, Abcam, Cat# ab13970, RRID:AB_300798), rabbit anti-PCCA (1:1000, NOVUSBIO, Cat# NBP2-32215), rabbit anti-GABAA1 (1:1000, EMD Millipore, Cat# 06-868, RRID:AB_310272), mouse anti-GluN2B (1:1000, Millipore Sigma, Cat# 05-920, RRID:AB_417391), rabbit anti-Prkaca (1:1000, Millipore Sigma, Cat# HPA071185, RRID:AB_2686356), rabbit anti-GluA2 (1:1000, Abcam, Cat# ab133477, RRID:AB_2620181), rabbit anti-SAPAP3 (1:1000, ThermoFisher scientific, Cat# 55056-1-AP, RRID:AB_10858793), rabbit anti-Homer1 (1:1000, Synaptic System, Cat# 160003, RRID:AB_887730), rabbit anti-SAP97 (1:1000, ThermoFisher scientific, Cat# PA1-741, RRID:AB_2092020), rabbit anti-GAPDH (1:2000, Cell Signaling Technology, Cat# 2118, RRID:AB_561053), rabbit anti-Shank1 (1:1000, Synaptic System, Cat# 162002), rabbit anti-Shank2 (1:1000, Cell Signaling Technology, Cat# 12218, RRID:AB_2797848), rabbit anti-Shank3 (1:1000, Boster Bio, Cat# A01231-1). After 3 ×10 min intense wash in TBST solution, membranes were incubated with corresponding secondary antibodies for one hour at RT with mild agitation. Following secondary

antibodies were used: goat-anti-rabbit poly-HRP (1:2000, Invitrogen, Cat# 32260, RRID:AB_1965959), goat-anti-mouse poly-HRP (1:2000, Invitrogen, Cat# 32230, RRID:AB_1965958) and goat-anti-chicken HRP (1:2000, Abcam, Cat# ab97135, RRID:AB_10680105). Then membranes were washed 3 ×10 min in TBST and developed with SuperSignal West Pico Chemiluminescent Substrate (Thermo Fisher, Cat# 34578) and imaged on a Chemidoc XRS system (Bio-Rad).

For Streptavidin-HRP blotting, membranes were blocked 10% biotin-free fetal bovine serum (FBS, Fisher Scientific, Cat# 26-400-044) in TBST solution overnight at 4 °C with mild agitation. Then membranes were incubated in streptavidin-horseradish peroxidase (1:50000, Life Technologies, Cat# 21130) for one hour at 4 °C with mild agitation. After 6 ×15 min intense wash in TBST solution, the blots were developed and imaged. Image Lab (Bio-Rad) and Fiji (NIH) were used for image analyses.

In-gel digestion

After CBB staining, a gel was cut into 11 slices based on protein molecular weight ladder (Biorad, Cat # 1610394). To separate major Shank3 protein isoforms into different gel slices, gel slices A and B were cut based on the observed Shank3 molecular weight from the WB analysis of WT SPN samples. Slice A includes top two Shank3 bands. Slice B only contains the third Shank3 band.

We performed in-gel digestions based on a widely-used protocol [19]. Briefly, each gel slice was put into a microcentrifuge tube and added 500 µl neat ACN to shrink the gel for 10 min. After removing ACN, DDT solution (10 mM DTT in 100 mM ammonium bicarbonate) was added. The tubes were incubated at 56 °C for 30 min. 500 µl neat ACN was added to remove extra DDT. Then, the gel slices were incubated with IAA (at RT) in dark for 20 min. After removing extra IAA, the gel slices were saturated with trypsin (13 ng/µl in 10 mM ammonium bicarbonate containing 10% ACN) and incubated at 37 °C overnight with intensive agitation. Peptides were extracted from gel slices by incubating with extraction solution (5% formic acid/ACN (1:2 vol/vol)) and vacuum centrifuged to dryness then desalted using ZipTips.

On-bead digestion

We performed on-beads digestion based on previous reported protocol [20]. After overnight incubation with striatal homogenates, NeutrAvidin beads were rinsed for five times in one ml lysis buffer (6 M Guanidine, 50 mM HEPES, pH8.5), then added one ml lysis buffer. Dithiothreitol (DTT, DOT Scientific Inc, Cat# DSD11000) was applied to a final concentration of 5 mM. After incubation at RT for 20 min, iodoacetamide (IAA, Sigma-Aldrich, Cat# I1149) was added to a final concentration of 15 mM and incubated for 20 min at RT in the dark. Excess IAA was quenched with DTT for 15 min. Samples were diluted with buffer (100 mM HEPES, pH 8.5, 1.5 M Guanidine), and digested for three hrs with Lys-C protease (1:100, ThermoFisher Scientific, Cat# 90307_3668048707) at 37 °C. Trypsin (1:100, Promega, Cat# V5280) was then added for overnight incubation at 37 °C with intensive agitation (1000 rpm). The next day, reaction was quenched by adding 1% trifluoroacetic acid (TFA, Fisher Scientific, O4902-100). The samples were desalted using HyperSep C18 Cartridges (Thermo Fisher Scientific, Cat# 60108-301) and vacuum centrifuged to dry.

Tandem Mass Tag (TMT) labeling

Our protocol was based on previously reported methods [21]. C18 column-desalted peptides were resuspended with 100 mM HEPES pH 8.5 and the concentrations were measured by micro BCA kit (Fisher Scientific, Cat# PI23235). For each sample, 25 µg of peptide labeled with TMT reagent (0.4 mg, dissolved in 40 µl anhydrous acetonitrile, Thermo Fisher Scientific, Cat# 90111) and made at a final concentration of 30% (v/v) acetonitrile (ACN). Following incubation at RT for 2 h with agitation, hydroxylamine (to a final concentration of 0.3% (v/v)) was added to quench the reaction for 15 min. For 3-plex TMT experiments, TMT-tagged samples were mixed at a 1:1:1 ratio. For 10-plex TMT experiments, TMT-tagged samples were mixed at a 1:1:1:1:1:1:1:1:1:1 ratio. Combined sample was vacuum centrifuged to dryness, resuspended, and subjected to HyperSep C18 Cartridges.

Peptide fractionation

We performed the strong cation exchange (SCX) fractionation for all 3-plex TMT-MS experiments. The desalted TMT-labeled sample was fractionated using Hypersep SCX columns (Thermo Fisher Scientific, Cat# 60108-420). Fractions were eluted twice in 300 µl buffer at increasing ammonium acetate concentrations (20, 50, 100, 500, 1000, 2000 mM ammonium acetate). Speed vacuumed to dryness then desalted by ZipTips (Pierce, Cat# 87784) and again dried down for a second time. For all 10-plex TMT-MS experiments, we used a high pH reverse-phase peptide fractionation kit (Thermo Fisher Scientific, Cat# 84868) to get eight fractions (5.0%, 10.0%, 12.5%, 15.0%, 17.5%, 20.0%, 22.5%, 25.0 and 50% of ACN in 0.1% triethylamine solution). The high pH peptide fractions were directly loaded into the autosampler for MS analysis without further desalting.

Mass spectrometry

Three micrograms of each fraction or sample were auto-sampler loaded with a Thermo EASY nLC 1000 UPLC pump or UltiMate 3000 HPLC pump onto a vented Acclaim Pepmap 100, 75 µm x 2 cm, nanoViper trap column coupled to a nanoViper analytical column (Thermo Fisher Scientific, Cat#: 164570, 3 µm, 100 Å, C18, 0.075 mm, 500 mm) with stainless steel emitter tip assembled on the Nanospray Flex Ion Source with a spray voltage of 2000 V. An Orbitrap Fusion (Thermo Fisher Scientific) was used to acquire all the MS spectral data. Buffer A contained 94.785% H2O with 5% ACN and 0.125% FA, and buffer B contained 99.875% ACN with 0.125% FA. For TMT MS experiments, the chromatographic run was for 4 hours in total with the following profile: 0–7% for 7, 10% for 6, 25% for 160, 33% for 40, 50% for 7, 95% for 5 and again 95% for 15 min receptively. For GeIC-MS^2, the chromatographic run was for 2 hours in total with the following profile: 2–8% for 6, 8–24% for 64, 24–36% for 20, 36–55% for 10, 55–95% for 10, 95% for 10 min.

We used a multiNotch MS3-based TMT method to analyze all the TMT samples [21–23]. The scan sequence began with an MS1 spectrum (Orbitrap analysis, resolution 120,000, 400-1400 Th, AGC target 2×10^5, maximum injection time 200 ms). MS2 analysis, 'Top speed' (2 s), Collision-induced dissociation (CID, quadrupole ion trap analysis, AGC 4×10^3, NCE 35, maximum injection time 150 ms). MS3 analysis, top ten precursors, fragmented by HCD prior to Orbitrap analysis (NCE 55, max AGC 5×10^4, maximum injection time 250 ms, isolation specificity 0.5 Th, resolution 60,000).

We used CID-MS2 method for GeLC-MS^2 experiments as previously described [24]. Briefly, ion transfer tube temp = 300 °C, Easy-IC internal mass calibration, default charge state = 2 and cycle time = 3 s. Detector type set to Orbitrap, with 60 K resolution, with wide quad isolation, mass range = normal, scan range = 300-1500 m/z, max injection time = 50 ms, AGC target = 200,000, microscans = 1, S-lens RF level = 60, without source fragmentation, and datatype = positive and centroid. MIPS was set as on, included charge states = 2–6 (reject unassigned). Dynamic exclusion enabled with n = 1 for 30 s and 45 s exclusion duration at 10 ppm for high and low. Precursor selection decision = most intense, top 20, isolation window = 1.6, scan range = auto normal, first mass = 110, collision energy 30%, CID, Detector type = ion trap, OT resolution = 30 K, IT scan rate = rapid, max injection time = 75 ms, AGC target = 10,000, Q = 0.25, inject ions for all available parallelizable time.

MS data analysis and quantification

Protein identification/quantification and analysis were performed with Integrated Proteomics Pipeline - IP2 (Bruker, Madison, WI. http://www.integratedproteomics.com/) using ProLuCID [25, 26], DTASelect2 [27, 28], Census and Quantitative Analysis (For TMT MS experiments). Spectrum raw files were extracted into MS1, MS2 and MS3 (For TMT experiments) files using RawConverter (http://fields.scripps.edu/downloads.php). The tandem mass spectra were searched against UniProt mouse protein database (downloaded on 10-26-2020) [29] and matched to sequences using the ProLuCID/SEQUEST algorithm (ProLuCID version 3.1) with 5 ppm peptide mass tolerance for precursor ions and 600 ppm for fragment ions. The search space included all fully and half-tryptic peptide candidates within the mass tolerance window with no-miscleavage constraint, assembled, and filtered with DTASelect2 through IP2. To estimate peptide probabilities and false-discovery rates (FDR) accurately, we used a target/decoy database containing the reversed sequences of all the proteins appended to the target database [30]. Each protein identified was required to have a minimum of one peptide of minimal length of six amino acid residues; however, this peptide had to be an excellent match with an FDR < 1% and at least one excellent peptide match. After the peptide/spectrum matches were filtered, we estimated that the peptide FDRs were ≤1% for each sample analysis. Resulting protein lists include subset proteins to allow for consideration of all possible protein forms implicated by at least two given peptides identified from the complex protein mixtures. Then, we used Census and Quantitative Analysis in IP2 for protein quantification of TMT MS. experiments and protein quantification was determined by summing all TMT report ion counts. TMT MS data were normalized using with a build-in method in IP2. For quantification of

phosphor-peptides, we calculated the reporter ion intensities from the phosphorylated and unmodified peptides within each protein using a compositional algorithm [31] to minimize distortion of the data. Briefly, for every phosphor-protein in each TMT channel, the total TMT reporter ion intensities of all peptides were added up to exactly 2,000,000 (missing values were treated as 0). Renormalized value for each peptide is calculated by the following formula:

TMT_x-Pi, the reporter ion intensity of peptide i inTMT x channel

Spyder (MIT, Python 3.7, libraries, 'pandas', 'numpy', 'scipy', 'statsmodels' and 'bioinfokit') was used for data analyses. RStudio (version, 1.2.1335, packages, 'tidyverse', 'pheatmap') was used for data virtualization. The Database for Annotation, Visualization and Integrated Discovery (DAVID) (https://david.ncifcrf.gov/) was used for protein functional annotation analysis.

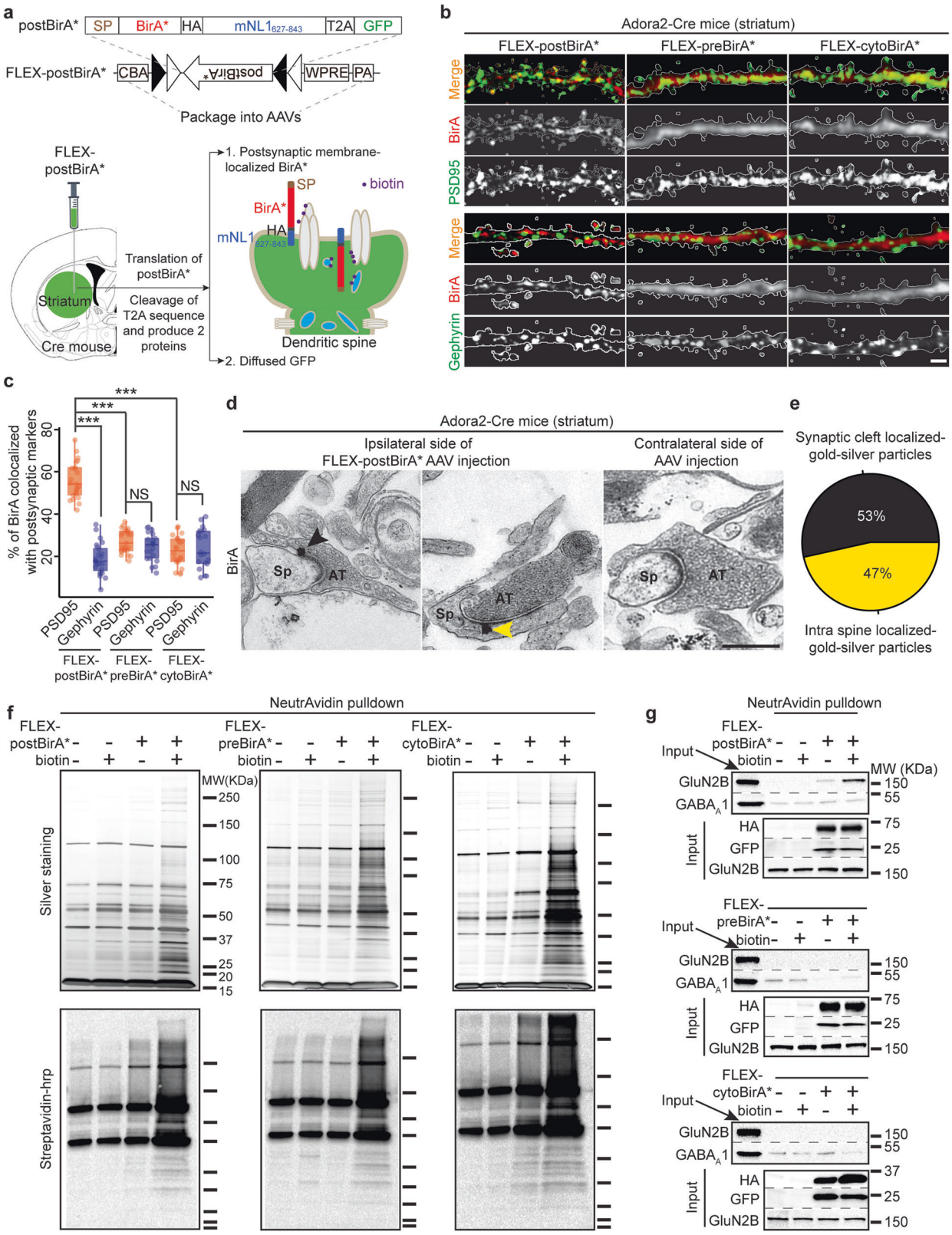

Fig. 1 Assessments of postBirA*-based in vivo proximity biotin-tagging toolkit. a *Top*, design of FLEX-postBirA* probe. SP, signal peptide, HA, human influenza hemagglutinin, 2 A, T2A self-cleavage oligopeptide, $mNL1_{627\text{-}843}$, mouse Neuroligin-1 (Uniprot ID, Q99K10) amino acid sequence 627-843 (includes transmembrane domain 698-718), CBA, chicken beta actin promotor, WPRE, Woodchuck hepatitis virus posttranscriptional regulatory element, PA, poly-A sequence. *Bottom*, schematics depict the intracranial injection of FLEX-postBirA* AAV into the striatum of a Cre-mouse, and the subsequent postsynaptic localization of BirA* driven by $mNL1_{627\text{-}843}$, which facilitates the proximity biotinylation of postsynaptic proteins. **b** Representative IHC analysis showing postBirA*, preBirA*, and cytoBirA* localization relative to the postsynaptic markers PSD95 or Gephyrin. BirA* expressing SPNs were identified based on co-expression of eGFP (white traces). Scale bar, 2 µm. **c** Quantification of (**b**). n = 4–6 mice, 3–5 brain slices from each mouse. One-tailed Student's t test, *** p value < 0.001. NS, not significant. **d** Representative immuno-EM micrographs demonstrating the postsynaptic localization of anti-BirA-gold-silver particles in Adora2-cre mouse striatum injected with FLEX-postBirA* AAVs (left & middle). No specifically localized anti-BirA-gold-silver particle was observed in the other striatum without AAV injection from the same mouse (right). Black arrow = synaptic cleft particle, yellow arrow = intra spine particle. Scale bar, 500 nm. Sp, spine, AT, axonal terminal. **e** Quantification of synaptic clefts containing gold-silver particles (23 out of 43, 53%) and intra spine (20 out of 43, 47%). **f** Biochemical analyses using silver staining (top) and Strepavidin-HRP blot (bottom) confirms that the three BirA* probes are enzymatically active in Adora2-Cre mouse striatum. **g** Excitatory postsynaptic protein GluN2B, but not inhibitory postsynaptic protein $GABA_A1$, is enriched in NeutrAvidin affinity purified material from postBirA* expressed striatum with biotin administration (top). Neither GluN2B nor $GABA_A1$ were specifically enriched in the affinity purified materials from striatum expressing either of the other two BirA* probes (middle and bottom).

SPN postsynaptic proteome library

Generation of training dataset: SynaptomeDB_Postsynaptic protein database [32] contains a broad

$$\frac{TMT_X - P_i}{\sum_{TMT_X - P_i \ldots \text{TMT}_a P_n}} \times 2000,000$$

range of postsynaptic proteins mostly discovered by proteomic methods. This database has a deep coverage of the postsynaptic proteome but also contains some misclassified presynaptic proteins. SynGO [33] is a smaller database and only contains experimentally validated synaptic proteins. Therefore, we combined these two databases to generate a large postsynaptic protein training dataset. Initially, we distinguished the presynaptic (SynGO_Presynapse) and postsynaptic proteins (SynGO_Postsynapse) within SynGO. Proteins associated with both pre- and postsynaptic areas were categorized as postsynaptic proteins and SynGO_Presynapse was reserved for proteins exclusively associated with the presynapse. Next, we refined the SynaptomeDB_Postsynaptic protein database by removing presynaptic proteins identified in SynGO_Presynapse, resulting in a cleaned SynaptomeDB_Postsynaptic protein list. Finally, we merged this cleaned list with SynGO_Postsynapse to create our comprehensive postsynaptic protein training dataset.

Random forest classifier: we used Python library 'sklearn' to build our classifier. Proteins were required to have two or more quantified peptides to be considered. For multiple protein isoforms assigned to one gene name, only the isoform with highest total TMT reporter ion intensity was considered. The following features of each protein were used for random forest classifications. They are 'spec count', 'sequence coverage', 'molecular weight', 'isoelectric point', '$\log_{10}$(total peptide intensity/protein length)', '$\text{Fold}_{\text{preBirA* TMT channel/cytoBirA* TMT channel}}$', '$\text{Fold}_{\text{postBirA* TMT channel/cytoBirA* TMT channel}}$', 'Normalized value in preBirA* TMT channel', 'Normalized value in cytoBirA* TMT channel' and 'Normalized value in postBirA* TMT channel'. Normalized values were calculated based on a previously reported way [20]. In summary, for each individual TMT channel, we used the median TMT reporter ion intensity of cytosolic and ER proteins as a normalization factor, selecting these proteins based on their GO annotations. Only those proteins identified as postsynaptic in at least two independent 3-plex TMT MS experiments were included in the SPN postsynaptic proteome library. ROC curves were plotted using RStudio. The developed SPN postsynaptic proteome library exhibits a false discovery rate (FDR) of 2.1% for non-synaptic membrane proteins and 2.2% for presynaptic proteins. It encompasses the majority of recognized excitatory postsynaptic proteins, including glutamate receptors and MAGUKs.

Shank3 protein isoform profiling

Standard Shank3 tryptic peptides: We generated theoretical Shank3 tryptic peptides for each Shank3 isoform listed in the UniProt database (A, B, C1, C3, D1, D2, E1, D2, and F) using the Fragment Ion Calculator online tool (http://db.systemsbiology.net:8080/proteomicsToolkit/FraglonServlet.html). Only fully tryptic Shank3 peptides were considered. Peptides longer than 35 or shorter than 8 amino acids (AA) were excluded, as they were not identified in any of our mass spectrometry (MS) experiments.

Shank3 gene exon mapping: We sequentially linked *Shank3* gene exons (NM_021423.4) from exon 1 to 22. The protein-coding sequence was determined by aligning it with Shank3A cDNA, which was then translated into amino acids (AA) using SnapGene Viewer (version 6.0.2). The N-terminal portions of Shank3B, C3, C4, D1, D2, E1, and E2 proteins are encoded by alternatively spliced transcripts. We in silico translated these mRNA transcripts and aligned our identified peptides to these sequences. For each gel slice, we considered only the Shank3 protein isoforms matching the expected molecular weight (MW). For example, full length Shank3A, with a theoretical MW of approximately 185.4 kDa, should only be present in gel band I. We then matched Shank3 tryptic peptide sequences with exon-mapped and alternative splicing transcript (AST)-derived AA sequences. This allowed us to map each Shank3 tryptic peptide to its corresponding exons and ASTs. Peptides covering AA sequences from two exons (exon-exon junctions) were labeled as 'A & B'.

Shank3 gene exon detection-frequency table: Utilizing the exon-mapping outcomes, we calculated the detection frequency of each exon (including alternative splicing transcripts, AST) or exon junction using the following formulas.

$$\frac{E_i}{\sum_{E_{I\ldots}\,E_m} + \sum_{E_{I\ldots}\,E_n}} \text{ or } \frac{EJ_i}{\sum_{E_{I\ldots}\,E_m} + \sum_{EJ_{I\ldots}\,EJ_n}}$$

E_i, number of detection events of exon (or AST) i. EJ_i, detection times of exon-joint i. Overall, we identified m exons (including ASTs) and n exon-joints. Consequently, for each GeLC-MS^2 experiment, we created a *Shank3* gene exon detection frequency table. Additionally, we compiled a standard *Shank3* gene exon detection frequency table for each Shank3 isoform listed in the UniProt database. We then employed t-distributed Stochastic Neighbor Embedding to analyze the similarities among all *Shank3* gene exon detection frequency tables. R packages 'readr' and 'Rtsne' were used to generate tSNE plots.

Quantification and statistical analysis

We did not use specific methods to determine sample size and confirm whether the data met the required criteria for our selected statistical techniques. Rather, we chose these techniques based on their common usage in previous studies within our field and their general acceptance in comparable experiments. For 3-plex TMT-MS experiments, mice and TMT channels were randomly assigned. For IHC, dendritic spine analysis and iEM, brain slices and secondary dendrites were randomly selected. For WB and silver/CBB staining, mice were randomly selected. Statistical significance was established through appropriate statistical tests, including one-tailed Student's t test, Fisher's exact test and two-way ANOVA. The variance is always considered dissimilar between the groups being statistically compared. The statistical details of experiments can be found in the figure legends, including, the name of statistical test, the number of replicates, and exact p-values. 'NS' for p value > 0.05, * for p value < 0.05, ** for p value < 0.01 and *** for p value < 0.001. All data points are presented in the figures. We only include postsynaptic proteins in the SPN postsynaptic proteome library. For all other experiments, no samples or animals were excluded from all other analyses. No binding was done.

RESULTS

Development of a toolkit for quantitative profiling of neuron-type-specific postsynaptic proteomes

To quantitatively profile cell-specific postsynaptic nano-environments, we designed a BirA* (postBirA*) probe to tag postsynaptic

proteins with biotin in vivo (Fig. 1a). We used mouse Nlgn1$_{627\text{-}843}$ (containing the transmembrane domain, Nlgn1$_{698\text{-}718}$) to target BirA* to the excitatory postsynaptic membrane [16]. The esterase domain of Nlgn1 was omitted to minimize potential effects on synapse composition by expression of postBirA* [34]. Upon expression, the T2A oligopeptide in the fusion protein will undergo cleavage, resulting in the formation of two proteins. The first protein has four elements: Signal Peptide (SP), BirA*, HA tag, and Nlgn1$_{698\text{-}718}$, which will anchor the probe to the postsynaptic membrane and facilitate protein biotinylation of proximal proteins (within approximately 10 nm). The second protein, GFP, will serve as a marker of expression. We also

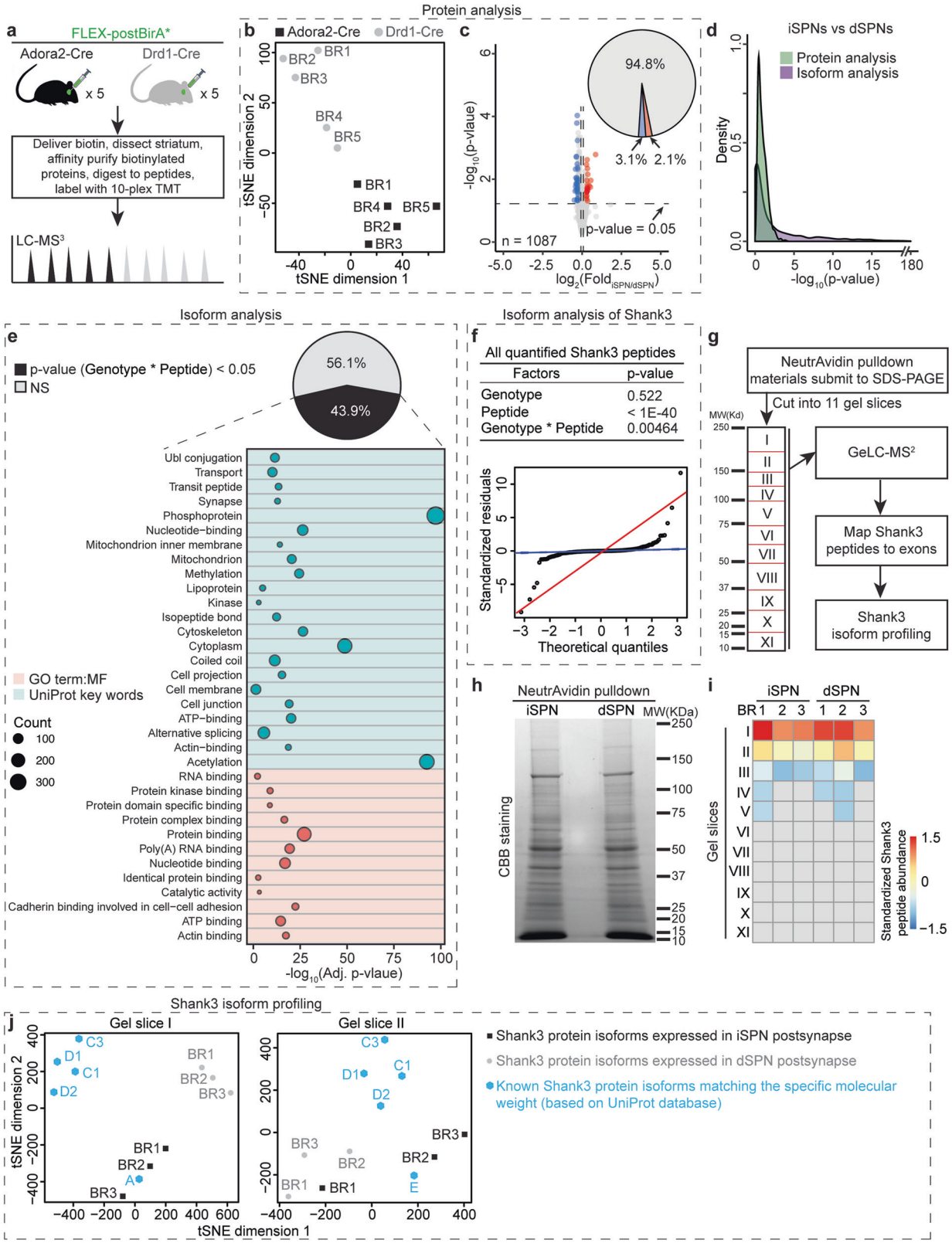

Fig. 2 Differences between iSPN and dSPN postsynaptic compartment proteomes are predominantly at the isoform level. a Experimental design to compare iSPN and dSPN postsynaptic compartment proteomes. n = 5 biological replicates (BRs) for each genotype. **b** Biological replicates cluster by genotype in (t-distributed stochastic neighbor embedding) tSNE plot based on protein analysis. **c** Volcano plot depicting comparison of iSPN and dSPN postsynaptic compartment proteomes based on protein analysis. Pie chart showing only ~5% proteins in iSPN postsynaptic compartment proteomes are differentially expressed in dSPNs. For proteins with multiple UniProt accessions, we only considered the accession with highest total TMT reporter ion intensity. See **Sheet1** in Table S2 for exact p value and the iSPN/dSPN ratio for each postsynaptic protein in the protein analysis. One-tailed Student's t test. **d** Isoform analysis revealed that the postsynaptic proteins were divergently expressed in iSPNs and dSPNs at isoform level. For protein analysis, p values were calculated by One-tailed Student's t test. For isoform analysis, p-values were calculated by two-way ANOVA. (PR > F): Genotype * peptide values were used. See **Sheet2** in Table S2 for exact p vlaue: C(Genotype), p-vlaue: C(Peptide) and p-vlaue: C(Genotype):C(Peptide) for each postsynaptic protein in the isoform analysis. **e** Gene functional classification analysis of postsynaptic proteins isoform-divergently expressed in iSPNs and dSPNs. For all listed terms, count > 30, adj. p value < 0.05. **f** Top, p values acquired by two-way ANOVA analysis of Shank3 peptides. Bottom, quantile-quantile (Q-Q) plots showing that the variances of Shank3 peptides in iSPNs and dSPNs are heteroscedastic. **g** Experimental design of GeLC-MS^2 based Shank3 protein isoform profiling. **h** Representative Coomassie blue (CBB) staining gels of NeutrAvidin affinity purified material from iSPN and dSPN samples. **i** Heatmap showing the distribution pattern of all identified Shank3 peptides in gel slices. See Table S3 for the exact sequence and mapped exon(s) of each identified Shank3 peptide in GeLC-MS^2 experiment. **j** Profiling of Shank3 protein isoforms in iSPNs and dSPNs postsynaptic compartments. *Left*, in gel slice I, the Shank3 protein isoform(s) expressed in iSPNs were closely-clustered with Shank3A. In contrast, the isoform(s) expressed in dSPNs were separated from others, suggesting there is unreported long Shank3 isoform(s) co-expressed with Shank3A in dSPNs. *Right*, in gel slice II, the isoforms expressed in dSPNs and iSPNs were loosely clustered with Shank3E.

constructed two negative control BirA* probes that localize to presynaptic membranes or the cytosol, preBirA* and cytoBirA*, respectively (Fig. S1a-b). We then sub-cloned all three BirA* probes into FLEX plasmids, allowing cell-type specific expression using adeno-associated virus (AAVs) vectors in transgenic mice expressing Cre recombinase under the control of cell-type specific promoters.

To use these tools to study cell-type specific synaptic proteomes, AAVs carrying the BirA* plasmids were stereotaxically injected into the striatum of Adora2-Cre mice, restricting their expression to A2a adenosine receptor expressing iSPNs [5, 6]. After one month, all three BirA* probes were robustly expressed in striatum (Fig. 1a, S1c). The postBirA* probe exhibited a punctate expression pattern in GFP-expressing iSPNs (Fig. 1b, S1d). In contrast, both the preBirA* and cytoBirA* probes had a diffuse expression pattern (Fig. 1b, S1d). The postBirA* puncta co-localized with excitatory postsynaptic marker PSD95, with significantly less colocalization with the inhibitory postsynaptic marker gephyrin (Fig. 1c). PostBirA* also was commonly juxtaposed with presynaptic vesicular glutamate transporter 1 (vGluT1) but not the vesicular GABA transporter (vGAT) (Fig. S1e). Thus, the postBirA* probe was enriched at the postsynaptic membrane of excitatory SPN synapses. By contrast, neither preBirA* nor cytoBirA* colocalized with PSD95, gephyrin, vGluT1 or vGAT (Fig. 1c, S1e).

Next, we performed immuno-electron microscopy (iEM) to confirm postsynaptic localization of postBirA* in SPNs (Fig. 1d, e, S1f). FLEX-postBirA* AAVs were injected into one striatum of Adora2-Cre mice and the other striatum was used as a negative control for iEM. Anti-BirA-gold-silver particles were found either in the synaptic cleft or within spine heads. Very few gold-silver particles were detected, and none localized to synapses in the uninfected striatum (Fig. 1d, S1f, right panels). Our iEM data strongly suggest that, when expressed in striatal SPNs, the biotin ligase domain of postBirA* is present at similar levels within the postsynaptic density and in spine heads. Since BirA* selectively biotinylates proteins in close physical proximity [15], our results suggested that postBirA* would predominantly biotinylate a broad spectrum of postsynaptic proteins in SPN glutamatergic synapses, including both transmembrane (e.g., AMPARs) and scaffolding proteins (e.g., PSD95).

Next, we examined the proteins biotinylated by each of BirA* probes in Adora2-Cre mice following subcutaneous injection of biotin or vehicle (i.e., saline) (Fig. 1f). Biotinylated proteins were affinity purified with NeutrAvidin agarose and the purified material was analyzed with SDS-PAGE and silver staining (Fig. 1f, top panels). Streptavidin-horseradish peroxidase blot was used to detect biotinylated proteins (Fig. 1f, bottom panels). Robust protein biotinylation signals were detected in the affinity-purified material from striata expressing the BirA* probes following biotin administration. For example, GluN2B, an NMDAR subunit known to be present at excitatory postsynapses, was only detected in the affinity-purified material from striata expressing postBirA* (Fig. 1g, top panel). The strongest GluN2B signal was detected in samples expressing postBirA* with biotin administration, while $GABA_A1$, a marker of inhibitory synapses was not enriched (Fig. 1g, top panel). Importantly, nearly no GluN2B signal was detected in samples purified from striata expressing preBirA* or cytoBirA* (Fig. 1g, S1g). We then used IHC to examine where the biotinylated proteins were localized. Notably, we found more biotin puncta colocalized with PSD95 in striata expressing postBirA* than in striata expressing the other probes (Fig. S1h). In summary, these results show that postBirA* can selectively biotinylate postsynaptic proteins at glutamatergic synapses in vivo.

Overexpression of postBirA* or preBirA* probes demonstrated no significant impact on synaptic transmission

We next examined whether postBirA* affects synaptic function when expressed in mouse striatum. To this end, we injected Cre-independent channelrhodopsin (ChR2) into primary motor cortex M1 of Adora2-Cre mice and FLEX-postBirA* or FLEX-cytoBirA* into dorsolateral striatum (DLS) of the same mice (Fig. S2a–c). Five weeks later, ex vivo brain slices were prepared from these mice and optogenetic methods used to activate corticostriatal glutamatergic axons while patch clamp recording from iSPNs in the DLS. The amplitude of light-induced excitatory postsynaptic currents (EPSCs) in postBirA* and cytoBirA* expressing SPNs was very similar (Fig. S2d). To examine SPN GABAergic synaptic transmission, Cre-independent ChR2 was co-injected with preBirA* or cytoBirA* into the striatum of Adora2-Cre mice (Fig. S2e, f). This led to robust expression of ChR2 in SPNs projecting to the GPe. In ex vivo brain slices from these mice, optogenetic methods were used to activate striatopallidal axons while recording from GPe neurons using patch clamp methods. The amplitude of inhibitory postsynaptic currents (IPSC) recorded in GPe neurons from preBirA* and cytoBirA* injected mice were indistinguishable (Fig. S2g, h). These findings suggest that our BirA* probes do not alter iSPN pre- or post-synaptic function.

Quantitative comparison of iSPN and dSPN postsynaptic proteomes

To quantitatively compare iSPN and dSPN postsynaptic compartment proteomes, we performed a postBirA*-based 10-plex TMT

mass spectrometry (MS) experiment (Fig. 2a). By injecting FLEX-postBirA* into the striatum of Adora2-Cre mice, its expression is limited to iSPNs that express the A2a adenosine receptor (Fig. S1c). Similarly, injecting FLEX-postBirA* into the striatum of Drd1-Cre mice confines its expression to dSPNs that express the dopamine receptor D1 (Fig. S3a) [5, 6]. To minimize the impact of harvesting extraneous proteins [35], a reference library of postsynaptic proteins was constructed by supervised machine learning (Fig. S3 and Table S1). Only proteins belonging to this library were considered relevant. As expected, the postsynaptic proteomes of iSPNs and dSPNs were similar (Fig. 2b, c, Table S2). However, there were differences in the protein abundance. For

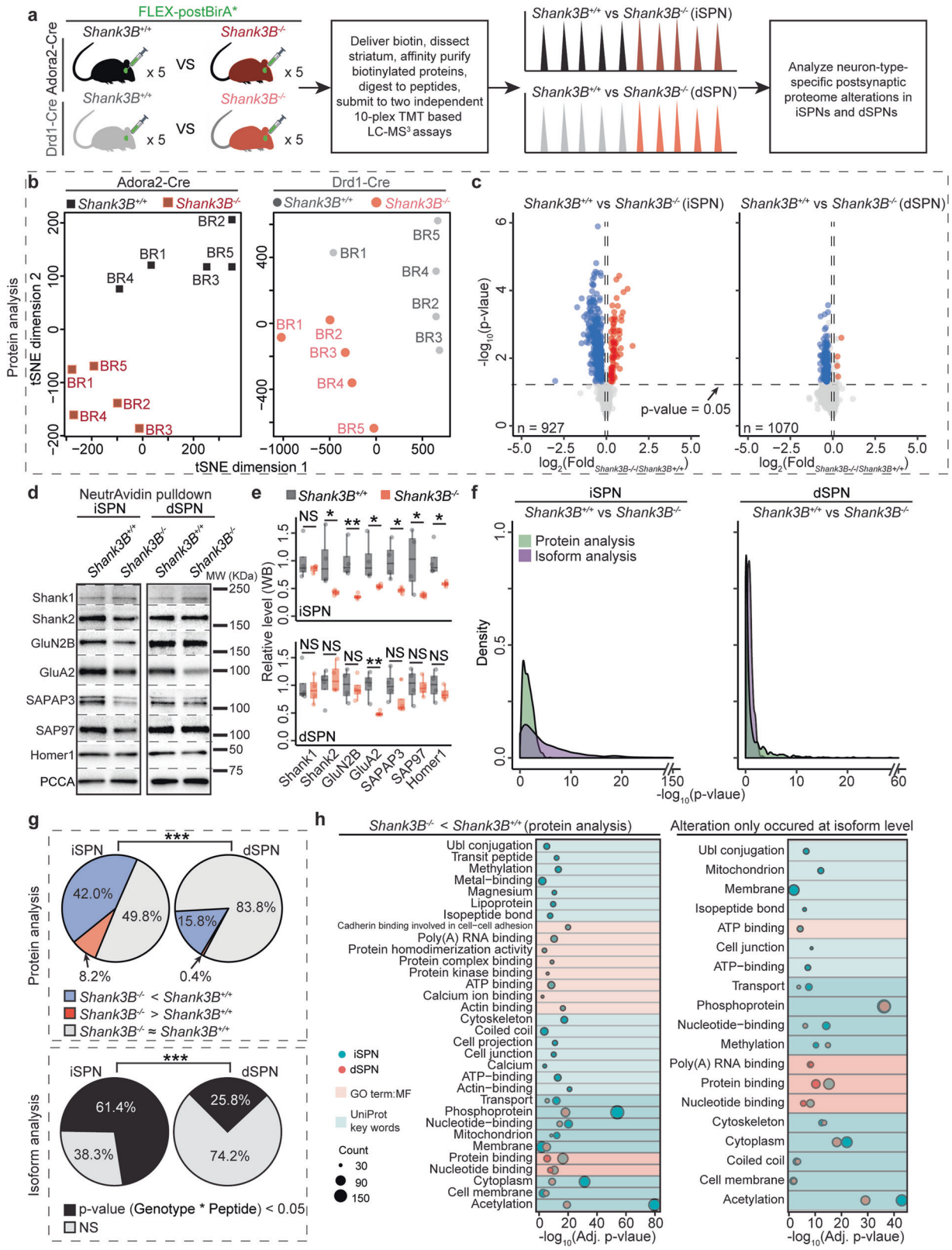

Fig. 3 Deletion of *Shank3* gene exons 13–16 divergently altered iSPN and dSPN postsynaptic compartment proteomes. a Experimental design to profile iSPN and dSPN postsynaptic compartment proteome alterations in *Shank3B*$^{-/-}$ mice. n = 5 biological replicates (BRs) for each genotype. **b** Biological replicates cluster by genotype in tSNE plots based on protein analysis. **c** Protein analysis revealed that ISPN postsynaptic compartment proteome was altered to a greater degree in *Shank3B*$^{-/-}$ mice compared to dSPNs. For proteins with multiple UniProt accessions, we only considered the accession with highest TMT reporter ion intensity. See **Sheet1 & 2** in Table S4 for exact p value and the *Shank3B*$^{-/-}$/*Shank3B*$^{+/+}$ ratio for each iSPN or dSPN postsynaptic protein in the protein analyses. One-tailed Student's t test. **d** SPN-type specific alterations of some proteins (Shank2, GluN2B, SAPAP3, SAP97 and Homer1) were validated by WB. GluA2 level was significantly reduced in both *Shank3B*$^{-/-}$ iSPNs and dSPNs compared to *Shank3B*$^{+/+}$ iSPNs. Shank3B deletion didn't alter Shank1 level in SPNs. **e** Quantification of (**d**), protein levels are normalized to PCCA. n = 4 mice per genotype. One-tailed Student's t test. **f** Exons 13–16 deletion led to a more robust iSPN postsynaptic protein expression alteration at isoform level compared to dSPN. For isoform analysis, p-values were calculated by two-way ANOVA. (PR > F): Genotype * peptide values were used. See **Sheet3 & 4** in Table S4 for exact p-vlaue: C(Genotype), p-vlaue: C(Peptide) and p-vlaue: C(Genotype):C(Peptide) for each postsynaptic protein in the isoform analyses. **g** Comparisons of postsynaptic protein alterations in *Shank3B*$^{-/-}$ iSPNs and dSPNs revealed by protein analysis and isoform analysis. Fisher's exact test. **h** Left, gene functional classification analysis of postsynaptic proteins significantly downregulated in *Shank3B*$^{-/-}$ iSPNs and dSPNs (protein analysis). Right, gene functional classification analysis of postsynaptic proteins which were differentially expressed (i.e. significantly) at isoform level in *Shank3B*$^{+/+}$ and *Shank3B*$^{-/-}$ SPNs. **e**, **g** * p value < 0.05, ** p value < 0.01, *** p value < 0.001, NS not significant.

example, the catalytic subunit of protein kinase A (Prkaca) was more abundant in the iSPN proteome than that of dSPNs [36, 37]. This difference was confirmed by WB and IHC (Fig. S4a–e). Additional evidence that this difference was of functional significance came from the discovery that there was a higher level of serine/threonine phosphorylated synaptic proteins in iSPNs than dSPNS (Figs. S5–6, Table S2).

Distinct Shank3 protein isoforms are expressed by iSPNs and dSPNs

Since ~70% of mammalian genes can produce multiple protein isoforms [38, 39], we hypothesized that traditional protein analysis workflow is not well suited to identify dissimilarities of SPNs at the protein isoform level (Fig. S5a). Therefore, a two-way ANOVA-based isoform analysis was used to compare iSPN and dSPN proteomes (Fig. 2d, Table S2). Surprisingly, nearly half (44%) of the synaptic proteomes of iSPNs and dSPNs differed at the isoform level (Fig. 2d, e, Fig. S5b-c). As different protein isoforms can have different functions [38], the disparity between iSPNs and dSPNs could have physiological consequences.

One of the most prominent differences between SPNs at the isoform level was for the postsynaptic scaffolding protein Shank3 [40–42] (Fig. 2f). Shank3 physically interconnects glutamate receptors with PSD-95 and Homer to the actin cytoskeleton and choreographs dendritic spine and synapse formation, maturation, maintenance, and plasticity. Shank3 gene mutations cause several neuronal developmental disorders, such as ASD, Phelan-McDermid syndrome (PMS), schizophrenia and intellectual disability (ID) [40, 41]. To validate this finding, we performed in-gel digestion coupled with mass spectrometric analysis (GeLC-MS2) to profile Shank3 protein isoforms in iSPNs and dSPNs (Fig. 2g–i, Fig. S7a). By denominational analysis of the identified Shank3 peptides in each gel piece, we found that the major long Shank3 isoforms expressed in iSPN and dSPNs postsynaptic proteomes differed (Fig. 2j, Fig. S7b, c, Table S3). The predominant long Shank3 protein isoform expressed in iSPNs and dSPNs was similar to Shank3A, but dSPNs also expressed another isoform(s). In contrast, iSPNs and dSPNs expressed similar short Shank3 protein isoforms.

Deletion of exons 13–16 in the *Shank3* gene distinctly alters the postsynaptic compartment proteomes of iSPNs and dSPNs

To explore the potential functional significance of this difference, *Shank3B*$^{-/-}$ mice were examined. *Shank3B*$^{-/-}$ mice have significant postsynaptic impairments in the striatum and display robust ASD-like behaviors, such as self-injurious grooming [43]. Therefore, our findings using this model should help guide the interpretation *Shank3B*$^{-/-}$ mouse phenotypes and may provide insight into human neurological conditions stemming from *Shank3 gene* mutations. In this mouse line, *Shank3* gene exons 13–16 have been replaced with a neomycin resistance cassette (Fig. S8a). Full-length Shank3A protein requires all 22 exons, while Shank3E protein is encoded by exons 17–22 [41, 44]. Thus, in *Shank3B*$^{-/-}$ mice, Shank3A was completely depleted while Shank3E remained [43]. Although Shank3C and D were also disrupted in this mouse line, their expression in striatum is very low and is not expected to play a major role in striatal synaptic function [40, 41, 45]. Two independent postBirA*-based 10-plex TMT MS experiments were performed to compare postsynaptic alterations in *Shank3B*$^{-/-}$ iSPNs and dSPNs (Fig. 3a). This analysis revealed that the iSPN postsynaptic proteome was more profoundly altered in *Shank3B*$^{-/-}$ mice than was that of dSPNs (Fig. 3b, c, Table S4). We further confirmed divergently regulated proteins identified through in vivo proximity biotin-tagging TMT experiments by WB (Fig. 3d, e). These results confirmed that the glutamatergic synaptic proteome of iSPNs was more dramatically altered than that of dSPNs (Fig. 3f–h, S8b, Table S4). These findings suggest that although Shank3A is a major postsynaptic scaffold in both iSPNs and dSPNs, dSPNs express another Shank3 isoform(s) that can partially compensate for the loss of Shank3A.

Distinct Shank3 protein isoforms are expressed in *Shank3B*$^{-/-}$ iSPNs and dSPNs

To test this hypothesis, we performed an additional isoform analysis of the *Shank3B*$^{-/-}$ postsynaptic proteomes. The relative abundance of Shank3 peptides was homoscedastic in *Shank3B*$^{-/-}$ iSPNs, but was highly heteroscedastic in *Shank3B*$^{-/-}$ dSPNs (Fig. 4a, S8c, Table S5). This result strongly suggests that the Shank3 protein isoforms in *Shank3B*$^{-/-}$ iSPNs and dSPNs were dissimilar. We further performed Shank3 WB analysis of NeutrAvidin agarose-affinity purified material from postBirA*-expressed striata (Fig. 4b). Interestingly, there was very little Shank3 signal in *Shank3B*$^{-/-}$ iSPNs. However, in *Shank3B*$^{-/-}$ dSPNs, several Shank3 protein isoforms were present. As there is not an antibody-based strategy that is able to detect all Shank3 protein isoforms, we performed GeLC-MS2 to profile the Shank3 protein isoforms in *Shank3B*$^{-/-}$ SPNs (Fig. 4c–e, S8d, Table S6). Notably, Shank3E was still expressed in *Shank3B*$^{-/-}$ dSPNs. We also identified two uncharacterized Shank3 isoforms in *Shank3B*$^{-/-}$ dSPNs, Shank3NT that was expressed at moderate levels and Shank3TL that was present in very low abundance. Moreover, the Shank3 proteins isoforms expressed in *Shank3B*$^{-/-}$ dSPNs contained all of the protein domains for cytoskeletal organization and Homer binding [41] (Fig. 4e). Consequently, we hypothesized that these isoforms are able to function as postsynaptic scaffolds and preserve dendritic spines in *Shank3B*$^{-/-}$ dSPNs (Fig. 4f). Our findings highlight that cell-type-specific Shank3 protein expression leads to a divergence in the impact of the *Shank3B*$^{-/-}$ deletion on iSPNs and dSPNs.

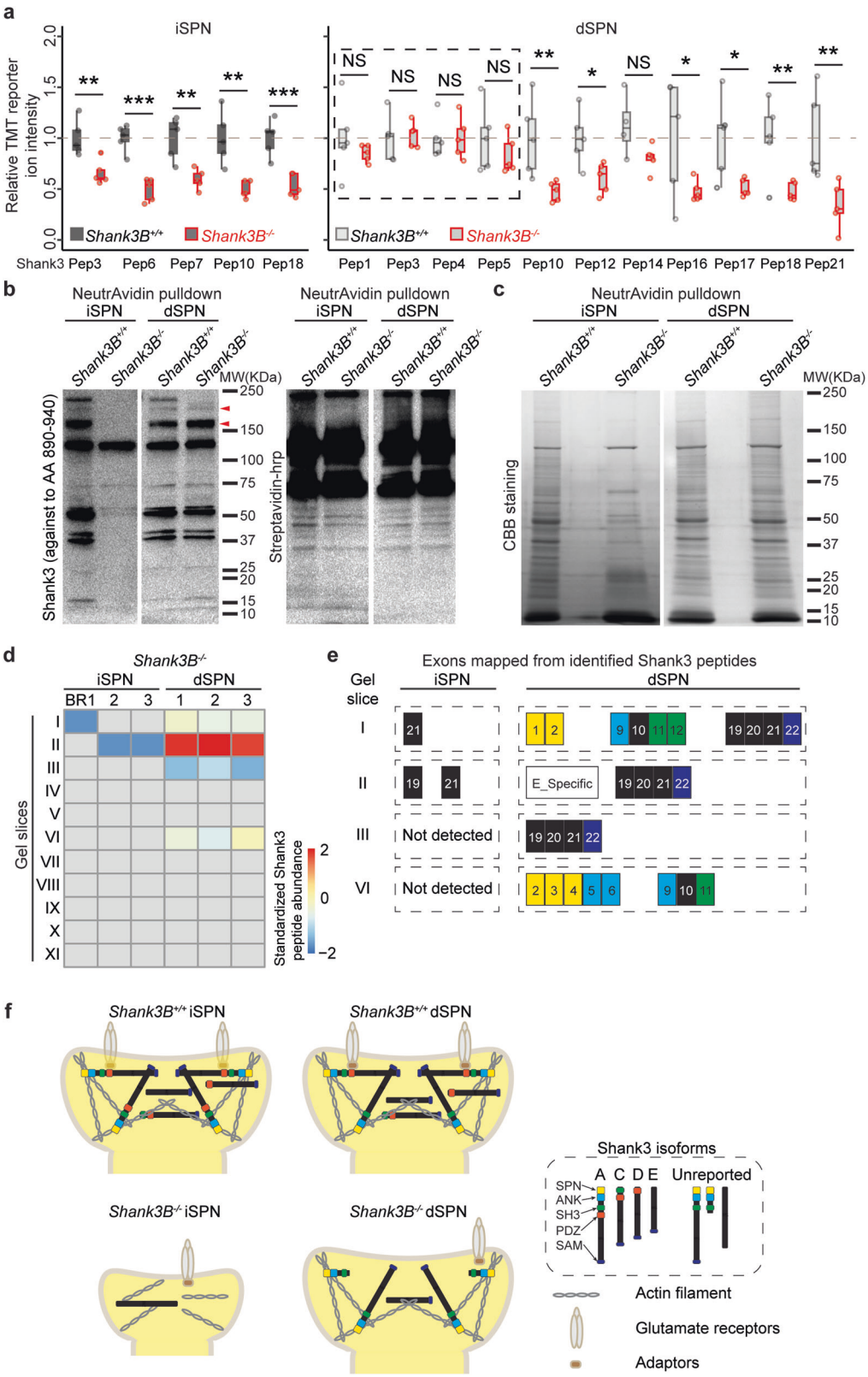

Selective iSPN synaptic deficits result from the deletion of exons 13–16 in the *Shank3* gene

To evaluate this hypothesis, AAVs containing the FLEX-GFP plasmid were stereotaxically injected into the striatum of *Adora2-Cre::Shank3B*$^{+/+}$, *Adora2-Cre::Shank3B*$^{-/-}$, *Drd1-Cre::Shank3B*$^{+/+}$, and *Drd1-Cre::Shank3B*$^{-/-}$ mice. This experiment aimed to specifically label *Shank3B*$^{+/+}$ iSPNs, *Shank3B*$^{-/-}$ iSPNs, *Shank3B*$^{+/+}$ dSPNs, and *Shank3B*$^{-/-}$ dSPNs, respectively (Fig. 5a). In line with our proteomic findings, the removal of exons 13–16 from the *Shank3* gene markedly decreases the dendritic spine density and the diameter

Fig. 4 Distinct Shank3 protein isoforms were expressed in dSPNs and iSPNs postsynaptic compartments. a The relative abundances of Shank3 peptides were homoscedastic in *Shank3B*$^{-/-}$ iSPNs but heteroscedastic in *Shank3B*$^{-/-}$ dSPNs. Pep = peptide. n = 5 mice per genotype. One-tailed Student's t test. See Table S5 for the exact sequence, p value and the *Shank3B*$^{-/-}$/*Shank3B*$^{+/+}$ ratio of each quantified Shank3 peptide in iSPNs and dSPNs. * p value < 0.05, ** p value < 0.01, *** p value < 0.001, NS, not significant. **b** Left, representative WB anlaysis of NeutrAvidin affinity purified material showed dissimilar Shank3 protein isoform expression patterns in *Shank3B*$^{-/-}$ SPNs. Three bands between 150-250 KDa in *Shank3B*$^{+/+}$ SPN samples are usually considered as Shank3A, 3 C/D and 3E. Arrow heads indicated Shank3 isoforms expressed in *Shank3B*$^{-/-}$ dSPN sample. Right, representative blots showed the level of all biotinylated protein as loading control. **c** Representative CBB staining gels of NeutrAvidin affinity purified material from the indicated SPN samples. **d** Shank3 peptides were identified at multiple gel slices. In *Shank3B*$^{-/-}$ iSPNs, we only identified a few Shank3 peptides in gel slices I and II. However, in *Shank3B*$^{-/-}$ dSPNs, Shank3 peptides were detected in gel slices I, II, III & VI. See Table S6 for the exact sequence and mapped exon(s) of each identified Shank3 peptide in GeLC-MS^2 experiment. **e** Identified Shank3 peptide amino acids were mapped to in silico translated *Shank3* gene exons (NM_021423.4). Each colored block represents a *Shank3* gene exon mapped from the identified peptides. Numbers in blocks, exon numbers. E_Specific, this peptide only belongs to Shank3E. Yellow, SPN domain, sky blue, ANK, green, SH3, dark blue, SAM. The data suggest that there may be an unreported long Shank3 isoform(s) in dSPN postsynaptic compartment which do not contain the PDZ domain (Shank3TL, in gel slice I). Notably, there we detected an unreported short Shank3 isoform (Shank3NT, in gel slice VI) in *Shank3B*$^{-/-}$ dSPN postsynaptic compartments, which contains SPN, ANK and SH3 domains. **f** Working model of the molecular mechanism underlying SPN-type-specific postsynaptic compartment impairments in *Shank3B*$^{-/-}$ striatum. ANK ankyrin repeats domain, SH3 src 3 domain, SAM sterile α motif domain, SPN N-terminal domain.

spines exclusively in iSPNs (Fig. 5b, c). However, we observed no significant morphological differences in the dendritic spines between *Shank3B*$^{+/+}$ and *Shank3B*$^{-/-}$ dSPNs. Moreover, there is no significant variation in the distribution of the three primary spine classes (mushroom, stubby, and thin/filopodia) between *Shank3B*$^{+/+}$ and *Shank3B*$^{-/-}$ SPNs (Fig. S9a).

To investigate the consequence of dendritic spine morphological deficits *in Shank3B*$^{-/-}$ iSPN on synaptic transmission, we further compared the corticostriatal inputs to *Shank3B*$^{+/+}$ and *Shank3B*$^{-/-}$ SPNs. First we injected Cre-independent channelrhodopsin (ChR2) into the primary motor cortex M1 of *Drd2-EGFP::Shank3B*$^{+/+}$ and *Drd2-EGFP::Shank3B*$^{-/-}$ mice (Fig. 5d, e). Five weeks later, ex vivo brain slices were prepared from these mice. Optogenetic techniques were then employed to stimulate corticostriatal glutamatergic axons while monitoring synaptic responses in DLS SPNs using patch-clamp recording. Both GFP-positive (iSPNs) and GFP-negative (dSPNs) were patched in the same slice to control for extraneous factors. The amplitude of light-induced EPSCs in *Shank3B*$^{-/-}$ iSPNs was significantly smaller than in *Shank3B*$^{+/+}$ iSPNs, *Shank3B*$^{+/+}$ and *Shank3B*$^{-/-}$ dSPNs (Fig. 5f, g). Conversely, the amplitude of light-induced EPSCs in *Shank3B*$^{+/+}$ and *Shank3B*$^{-/-}$ dSPNs was similar. These findings reveal that both spine morphology and corticostriatal synaptic function of iSPNs in the *Shank3B*$^{-/-}$ striatum were selectively compromised. These results additionally reinforce our hypothesis that Shank3 protein isoforms in *Shank3B*$^{-/-}$ dSPNs maintain spine morphology and preserve specific synaptic functions.

Overexpression of Shank3E1 in striatal iSPNs of adult *Shank3B*$^{-/-}$ mice ameliorates synaptic deficits

To test this hypothesis, we expressed the Shank3 protein isoforms identified in *Shank3B*$^{-/-}$ in *Shank3B*$^{-/-}$ iSPNs to determine whether the synaptic deficits were rescued. We found that two major Shank3 protein isoforms, Shank3E and Shank3NT, were expressed in *Shank3B*$^{-/-}$ dSPNs, but were undetectable in *Shank3B*$^{-/-}$ iSPNs. (Fig. 4c–e, S8d, Table S6). Additionally, a few very low-abundance Shank3 isoforms were expressed in *Shank3B*$^{-/-}$ iSPNs (Table S6). These isoforms do not contain any new functional domains compared to Shank3E and Shank3NT. Consequently, we didn't anticipate that these isoforms would play a significant role in maintaining spine morphology and synaptic function. Thus, we generated AAVs carrying FLEX-Vector (translation product: GFP), FLEX-Shank3E1 (translation products: mouse Shank3E1, UniProt ID: Q4ACU6-9 and GFP), and FLEX-Shank3NT (translation products from *Shank3* gene exons 1-12 and GFP) (Fig. S9b), which we then stereotaxically injected into the striatum of approximately three-month-old *Adora2a-Cre::Shank3B*$^{-/-}$ mice. Furthermore, to investigate potential combinatorial effects between Shank3E1 and Shank3NT, we pooled the FLEX-Shank3E1 and FLEX-Shank3NT AAVs and administered the mixture to the mice.

These experiments revealed that the overexpression of Shank3E1 enhanced the density of mushroom spines in *Shank3B*$^{-/-}$ iSPNs (Fig. 6a, b). Overexpression also led to an increase in the spine head diameter of all three primary spine classes (Fig. 6c) and mildly elevated the proportion of mushroom spines among these classes (Fig. 6d). Interestingly, expression of Shank3NT reduced spine density while substantially increasing spine head diameter. Yet, when Shank3NT was co-expressed with Shank3E1, it had little effect on spine morphology (Fig. 6).

To determine if overexpressing Shank3E1 rescued corticostriatal synaptic function in *Shank3B*$^{-/-}$ iSPNs, we injected Cre-independent channelrhodopsin (ChR2) into the primary motor cortex M1 and FLEX-Shank3E1 into the striatum of approximately three-month-old *Adora2a-Cre::Shank3B*$^{-/-}$ mice (Fig. 6e, f). Both GFP-positive (iSPNs) and GFP-negative (dSPNs) were patched in the same slice to control for extraneous factors. The amplitude of light-induced EPSCs in GFP-positive *Shank3B*$^{-/-}$ iSPNs expressing Shank3E1 is comparable to that in GFP-negative *Shank3B*$^{-/-}$ dSPNs (Fig. 6g, h), demonstrating that expression of Shank3E1 restored synaptic function. Thus, overexpression of Shank3E1 in *Shank3B*$^{-/-}$ rescues iSPN synaptic defects.

DISCUSSION

We have developed a toolkit to quantitatively profile neuron type-specific postsynaptic proteomes in vivo. Using these tools, we discovered that at the protein level dSPN and iSPN postsynaptic proteomes are highly similar. However, at the protein isoform level we unexpectedly found significant differences. In particular, Shank3, a critical postsynaptic scaffolding protein, is expressed as distinct proteoforms in *Shank3B*$^{-/-}$ iSPNs and dSPNs. Such diversity in the expression of Shank3 proteoforms may lead to cell type specific synaptic impairments in *Shank3B*$^{-/-}$ iSPNs and dSPNs. Consistently, we found that *Shank3B*$^{-/-}$ iSPNs have reduced dendritic spine density and smaller spine heads compared to *Shank3B*$^{-/-}$ dSPNs. The corticostriatal input to *Shank3B*$^{-/-}$ iSPNs was also significantly weaker than that to *Shank3B*$^{-/-}$ dSPNs. Importantly, these selective synaptic deficits are rectified by expression of Shank3E1 in *Shank3B*$^{-/-}$ iSPNs. In summary, our results suggest that the diversity of Shank3 proteoforms in iSPNs and dSPNs leads to the cell type-specific striatal synaptopathy in *Shank3B*$^{-/-}$ mice. This phenomenon may be a key contributor to the autistic behaviors, particularly repetitive self-injurious grooming, in this ASD mouse model.

Our study is not without some limitations and the over-expression of our BirA* probes might induce changes in the synaptic proteome. It is important to note that BirA*-based proximity biotinylation (e.g., BioID) has already been successfully used to characterize several distinct synaptic proteomes in vivo

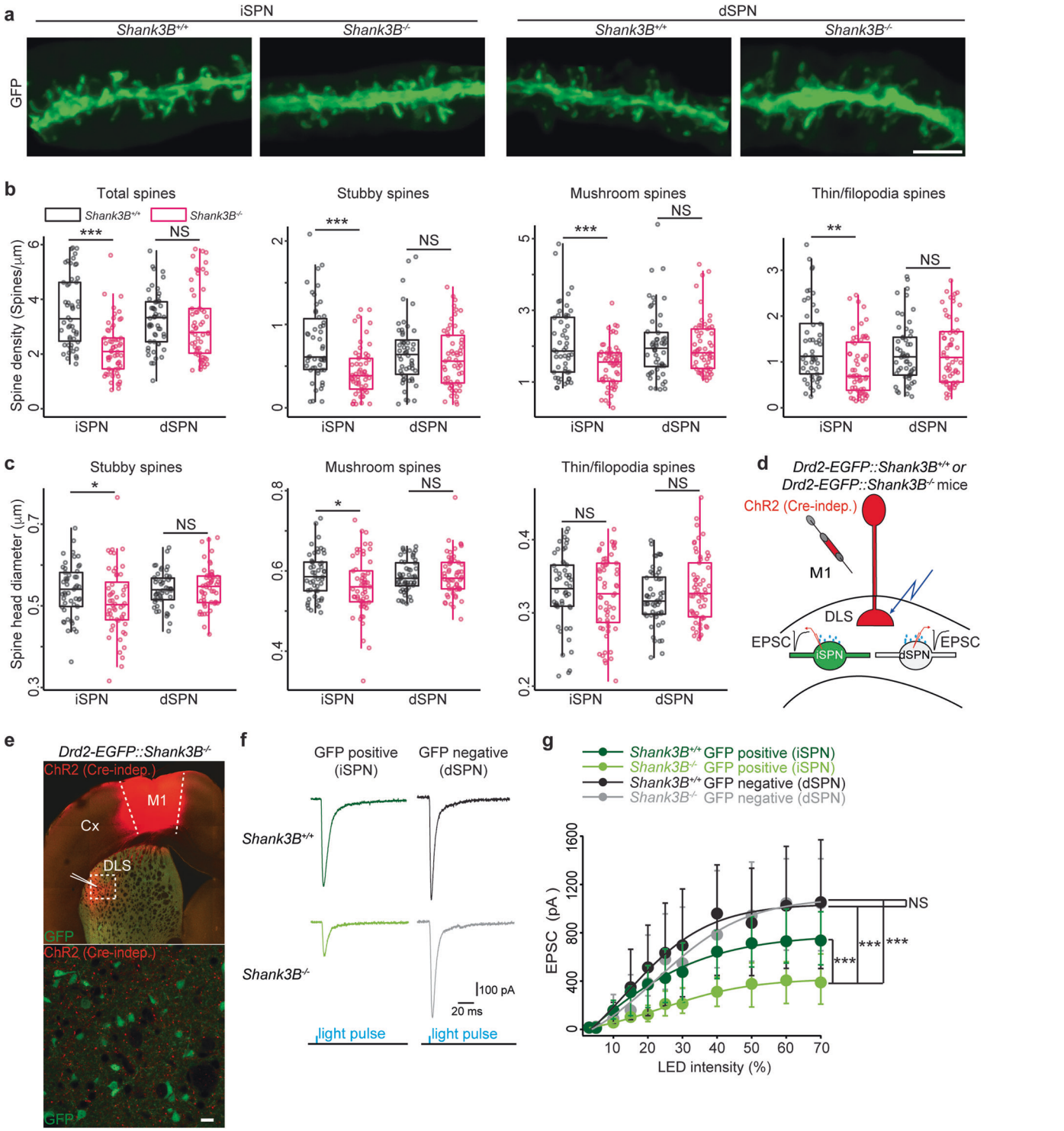

Fig. 5 Mice lacking exons 13–16 in the *Shank3* gene have synaptic impairments selectively in iSPNs. a Representative images displaying SPN dendrites from mice with the specified genotypes. Scale bar, 4 μm. Analysis of spine density (**b**) and spine head diameter (**c**) across three primary spine types in SPN dendrites from mice of the indicated genotypes. n = 5 mice per genotype, 10–14 dendritic fragments per mice. One-tailed Student's t test. * p value < 0.05, ***, p value < 0.001, NS, no significance. **d** Diagram showing the experimental design. ChR2 (cre-indep.), Cre-independent Channelrhodopsin-2, Cx cortex, M1 primary motor cortex, DLS dorsolateral striatum, EPSC excitatory postsynaptic current. **e** *Top*, low magnification confocal imaging showing ChR2 expression (mCherry) in M1 cortex and DLS, and GFP expression of the striatal iSPNs. *Bottom*, high magnification confocal imaging of an area within the white dotted line frame from the upper image. Scale bar, 15 μm. **f** Representative EPSC responses in GFP-positive or -negative striatal SPNs from mice with the specified genotypes. **g** Input/output curves for the peak of corticostriatal EPSCs responses (Vm = -80 mV). EPSC are significantly reduced in *Shank3B*$^{-/-}$ iSPNs (GFP-positive) but not in *Shank3B*$^{-/-}$ dSPNs (GFP-negative), at 30% LED intensity. *Shank3B*$^{-/-}$ iSPNs (GFP-positive): -212 pA (n = 6, 6 mice), *Shank3B*$^{-/-}$ dSPNs (GFP-negative): - 548 pA (n = 6, 6 mice), *Shank3B*$^{+/+}$ iSPNs (GFP-positive): -476 pA (n = 7, 6 mice), *Shank3B*$^{+/+}$ dSPNs (GFP-negative): -696 pA (n = 6, 5 mice). Two-way ANOVA, ***p < 0.0001. NS no significance.

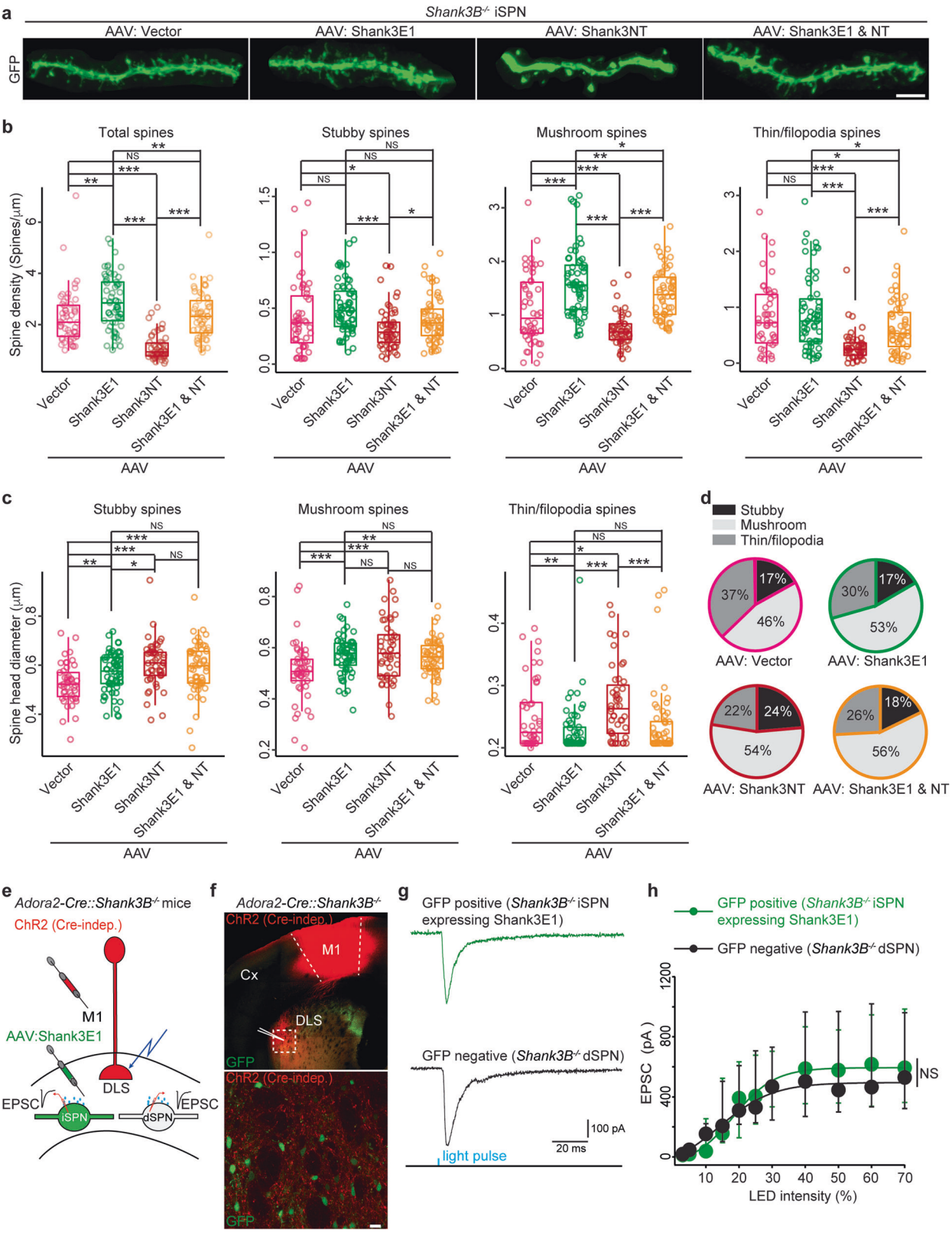

[17, 46–48]. In a recent publication, the possibility that BirA* may be toxic to mammalian cells has been tested and it has been confirmed that it is non-toxic [49]. The post synaptic targeting motif (i.e., $Nlgn1_{698\text{-}718}$), was chosen since it was originally used in the mGRASP system to map neural circuits [16, 50]. As an alternative approach to protein proximity biotinylation-based strategies, endogenous proteins can also be epitope tagged and used for affinity purification in combination with MS analysis to study synapse specific proteomes [51]. Transcriptomic techniques, particularly long-read single-cell RNA and single-nuclei RNA

Fig. 6 Overexpression of Shank3E1 in *Shank3B*$^{-/-}$ iSPNs rescues synaptic deficits. a Example images display typical SPN dendrites from *Adora2-Cre::Shank3B*$^{-/-}$ mice injected with the specified AAVs in striatum. Scale bar, 4 μm. Analysis of spine density (**b**) and spine head diameter (**c**) across three primary spine types in SPN dendrites from *Adora2-Cre::Shank3B*$^{-/-}$ mice injected with the specified AAVs in striatum. n = 5 mice per genotype, 10–15 dendritic fragments per mice. One-tailed Student's t test. * p value < 0.05, ***, p value < 0.001, NS, no significance. **d** Proportional distribution of three main spine types in SPN dendrites from *Adora2-Cre::Shank3B*$^{-/-}$ mice injected with the specified AAVs in striatum. **e** Diagram showing the experimental design. **f** *Top*, low magnification confocal image showing ChR2 expression (indicated by mCherry) in M1 cortex and DLS, and expression of Shank3E1 (indicated by GFP) in striatal *Shank3B*$^{-/-}$ iSPNs. *Bottom*, high magnification confocal image of an area within the white dotted line frame from the upper image. Scale bar, 15 μm. **g** Representative EPSC responses in specified SPNs. **h** Input/output curves for the peak of corticostriatal EPSCs responses (Vm = -80 mV). Injection of the Shank3E viral construct rescues EPSC on *Shank3B*$^{-/-}$ iSPNs (GFP-positive), at 30% LED intensity; *Shank3B*$^{-/-}$ iSPNs (GFP-positive): -469 pA (n = 7, 6 mice), mostly *Shank3B*$^{-/-}$ dSPNs (GFP-negative): - 468 pA (n = 8, 6 mice). Two-way ANOVA, NS, no significance, p value = 0.5590.

sequencing can also be effective approaches and complement proteomic datasets [52, 53]. These transcriptomic methods can simultaneously analyze many cell types in a single experiment within a relatively short timeframe, with almost no constraints on the amount of the sample needed. In contrast, our proteomic approach demands a substantially larger quantity of sample (i.e., biotinylated proteins). It is also unable to identify protein isoforms that are present in extremely low concentrations. Our strategy is also more time-consuming than transcriptomic techniques and typically can analyze only a few cell types at a time. However, our method provides accurate quantitative measures of proteins levels with cell type-specific subcellular resolution.

Individuals with *Shank3* gene mutations display a wide range of clinical symptoms [40, 41, 54]. Patients with Phelan-McDermid syndrome, which have only one copy of the *Shank3* gene, suffer from developmental delay, hypotonia, delayed or absent speech, and autistic symptoms such as restricted and repetitive behaviors. Additional *Shank3* gene mutations, such as nonsense mutations, are commonly observed in ASD and ID patients. Similarly, ASD mouse models with *Shank3* gene mutations manifest some ASD-like deficits, but also have a wide range of neurological phenotypes. This phenotypic heterogeneity has been hypothesized to be due to the expression pattern of Shank3 protein isoforms and their complex impact on postsynaptic proteomes [45, 55]. Consistent with this thesis, we found clear differences between iSPNs and dSPNs in their expression of Shank3 protein isoforms. In iSPNs, Shank3A is the predominant isoform and includes all the functional domains (i.e., SPN, ANK, SH3, PDZ, PRO, and SAM) [40, 41]. However, in dSPNs, additional shorter Shank3 isoforms such as Shank3E are also expressed and only contains the PRO and SAM domains. The deletion of exons 13–16 in the *Shank3* gene, which code for the PDZ domain, does not eliminate Shank3E expression. Shank3E in *Shank3B*$^{-/-}$ dSPNs acts as an incomplete postsynaptic scaffold, helping to maintain dendritic spine morphology and can sustain synaptic function to at least some extent (Fig. 5 & 6). In contrast, deletion of exons 13–16 in the *Shank3* gene in iSPNs suppresses expression of all the major Shank3 isoforms, leading to more severe synaptic deficits than those observed in *Shank3B*$^{-/-}$ dSPNs. These results are consistent with recent work showing that the synaptic impairment in *Shank3B*$^{-/-}$ mice is distinct between iSPNs and dSPNs [56]. Notably, Shank3 is widely expressed throughout the brain and exhibits distinct patterns of isoform specific expression in several regions [40, 41]. Consequently, removing exons 13–16 from the *Shank3* gene causes significant disruptions in various neuronal circuits in brain regions including hippocampus [57], the prefrontal cortex [58], and anterior cingulate cortex [59]. These circuit dysfunctions lead to diverse symptoms observed in *Shank3B*$^{-/-}$ mice. Investigating the contributions of Shank3 isoforms in additional neuron types and exploring their involvement in the malfunctioning of related neuronal circuits is significant for future studies.

There is a growing body of evidence showing a strong association between expression of mRNA transcripts encoding distinct protein isoforms and neuropsychiatric disorders [60–62]. Many additional synaptic genes that are associated with these disorders, such as *Syngap1* [63], *Kalrn* [64], *Nlgns*, and *Nrxns* [65] are also expressed in multiple proteoforms. Therefore, the pathological mutation of these risk genes may also lead to protein isoform imbalances and postsynaptic proteome alterations in a neuron-type-specific manner. Our methodology can be used to examine neuron-type-specific protein expression patterns and direct pharmaco- and genetic therapies for treating neuronal disorders, such as ASD in future studies.

DATA AVAILABILITY

The mass spectrometry data presented in this study was deposited in Mass Spectrometry Interactive Virtual Enviroment (MassIVE) under the identifier MSV000094094 and ProteomeXchange under the identifier PXD049408. The code used for random forest classifier is available in https://github.com/Tosfly/MolPsy2024.

REFERENCES

1. Grant SGN, Fransen E. The synapse diversity dilemma: molecular heterogeneity confounds studies of synapse function. Front Synaptic Neurosci. 2020;12:590403.
2. Cizeron M, Qiu Z, Koniaris B, Gokhale R, Komiyama NH, Fransen E, et al. A brainwide atlas of synapses across the mouse life span. Science. 2020;369:270–5.
3. Zhu F, Cizeron M, Qiu Z, Benavides-Piccione R, Kopanitsa MV, Skene NG, et al. Architecture of the mouse brain synaptome. Neuron. 2018;99:781–99.e710.
4. Emes RD, Grant SG. Evolution of synapse complexity and diversity. Annu Rev Neurosci. 2012;35:111–31.
5. Gerfen CR, Surmeier DJ. Modulation of striatal projection systems by dopamine. Annu Rev Neurosci. 2011;34:441–66.
6. Tritsch NX, Sabatini BL. Dopaminergic modulation of synaptic transmission in cortex and striatum. Neuron. 2012;76:33–50.
7. Kreitzer AC. Physiology and pharmacology of striatal neurons. Annu Rev Neurosci. 2009;32:127–47.
8. Blumenstock S, Dudanova I. Cortical and striatal circuits in Huntington's disease. Front Neurosci. 2020;14:82.
9. Zhai S, Tanimura A, Graves SM, Shen W, Surmeier DJ. Striatal synapses, circuits, and Parkinson's disease. Curr Opin Neurobiol. 2018;48:9–16.
10. Fuccillo MV. Striatal circuits as a common node for autism pathophysiology. Front Neurosci. 2016;10:27.
11. Day M, Wang Z, Ding J, An X, Ingham CA, Shering AF, et al. Selective elimination of glutamatergic synapses on striatopallidal neurons in Parkinson disease models. Nat Neurosci. 2006;9:251–9.
12. Rothwell PE, Fuccillo MV, Maxeiner S, Hayton SJ, Gokce O, Lim BK, et al. Autism-associated neuroligin-3 mutations commonly impair striatal circuits to boost repetitive behaviors. Cell. 2014;158:198–212.
13. Bergonzoni G, Doring J, Biagioli M. D1R- and D2R-medium-sized spiny neurons diversity: insights into striatal vulnerability to Huntington's disease mutation. Front Cell Neurosci. 2021;15:628010.
14. Wang YZ, Savas JN. Uncovering discrete synaptic proteomes to understand neurological disorders. Proteomes. 2018;6:30.
15. Roux KJ, Kim DI, Raida M, Burke B. A promiscuous biotin ligase fusion protein identifies proximal and interacting proteins in mammalian cells. J Cell Biol. 2012;196:801–10.
16. Kim J, Zhao T, Petralia RS, Yu Y, Peng H, Myers E, et al. mGRASP enables mapping mammalian synaptic connectivity with light microscopy. Nat Methods. 2011;9:96–102.
17. Uezu A, Kanak DJ, Bradshaw TW, Soderblom EJ, Catavero CM, Burette AC, et al. Identification of an elaborate complex mediating postsynaptic inhibition. Science. 2016;353:1123–9.
18. Wright WJ, Graziane NM, Neumann PA, Hamilton PJ, Cates HM, Fuerst L, et al. Silent synapses dictate cocaine memory destabilization and reconsolidation. Nat Neurosci. 2020;23:32–46.

19. Shevchenko A, Tomas H, Havlis J, Olsen JV, Mann M. In-gel digestion for mass spectrometric characterization of proteins and proteomes. Nat Protoc. 2006;1:2856–60.
20. Loh KH, Stawski PS, Draycott AS, Udeshi ND, Lehrman EK, Wilton DK, et al. Proteomic analysis of unbounded cellular compartments: synaptic clefts. Cell. 2016;166:1295–1307.e1221.
21. Weekes MP, Tomasec P, Huttlin EL, Fielding CA, Nusinow D, Stanton RJ, et al. Quantitative temporal viromics: an approach to investigate host-pathogen interaction. Cell. 2014;157:1460–72.
22. McAlister GC, Nusinow DP, Jedrychowski MP, Wuhr M, Huttlin EL, Erickson BK, et al. MultiNotch MS3 enables accurate, sensitive, and multiplexed detection of differential expression across cancer cell line proteomes. Anal Chem. 2014;86:7150–8.
23. Ting L, Rad R, Gygi SP, Haas W. MS3 eliminates ratio distortion in isobaric multiplexed quantitative proteomics. Nat Methods. 2011;8:937–40.
24. Savas JN, Wang YZ, DeNardo LA, Martinez-Bartolome S, McClatchy DB, Hark TJ, et al. Amyloid accumulation drives proteome-wide alterations in mouse models of Alzheimer's disease-like pathology. Cell Rep. 2017;21:2614–27.
25. Eng JK, McCormack AL, Yates JR. An approach to correlate tandem mass spectral data of peptides with amino acid sequences in a protein database. J Am Soc Mass Spectrom. 1994;5:976–89.
26. Xu T, Park SK, Venable JD, Wohlschlegel JA, Diedrich JK, Cociorva D, et al. ProLuCID: An improved SEQUEST-like algorithm with enhanced sensitivity and specificity. J Proteomics. 2015;129:16–24.
27. Cociorva D, Tabb DL, Yates JR. Validation of tandem mass spectrometry database search results using DTASelect. Curr Protoc Bioinformatics. 2007; Chapter 13: Unit 13 14.
28. Tabb DL, McDonald WH, Yates JR 3rd. DTASelect and Contrast: tools for assembling and comparing protein identifications from shotgun proteomics. J Proteome Res. 2002;1:21–26.
29. UniProt C. UniProt: a hub for protein information. Nucleic Acids Res. 2015;43:D204–D12.
30. Peng J, Elias JE, Thoreen CC, Licklider LJ, Gygi SP. Evaluation of multidimensional chromatography coupled with tandem mass spectrometry (LC/LC-MS/MS) for large-scale protein analysis: the yeast proteome. J Proteome Res. 2003;2:43–50.
31. Jovanovic M, Rooney MS, Mertins P, Przybylski D, Chevrier N, Satija R, et al. Immunogenetics. Dynamic profiling of the protein life cycle in response to pathogens. Science. 2015;347:1259038.
32. Pirooznia M, Wang T, Avramopoulos D, Valle D, Thomas G, Huganir RL, et al. SynaptomeDB: an ontology-based knowledgebase for synaptic genes. Bioinformatics. 2012;28:897–9.
33. Koopmans F, van Nierop P, Andres-Alonso M, Byrnes A, Cijsouw T, Coba MP, et al. SynGO: an evidence-based, expert-curated knowledge base for the synapse. Neuron. 2019;103:217–34.e214.
34. Dean C, Dresbach T. Neuroligins and neurexins: linking cell adhesion, synapse formation and cognitive function. Trends Neurosci. 2006;29:21–29.
35. Tytgat HL, Schoofs G, Driesen M, Proost P, Van Damme EJ, Vanderleyden J, et al. Endogenous biotin-binding proteins: an overlooked factor causing false positives in streptavidin-based protein detection. Microb Biotechnol. 2015;8:164–8.
36. Iino Y, Sawada T, Yamaguchi K, Tajiri M, Ishii S, Kasai H, et al. Dopamine D2 receptors in discrimination learning and spine enlargement. Nature. 2020;579:555–60.
37. Lee SJ, Lodder B, Chen Y, Patriarchi T, Tian L, Sabatini BL. Cell-type-specific asynchronous modulation of PKA by dopamine in learning. Nature. 2021;590:451–6.
38. Raj B, Blencowe BJ. Alternative splicing in the mammalian nervous system: recent insights into mechanisms and functional roles. Neuron. 2015;87:14–27.
39. Aebersold R, Agar JN, Amster IJ, Baker MS, Bertozzi CR, Boja ES, et al. How many human proteoforms are there? Nat Chem Biol. 2018;14:206–14.
40. Jiang YH, Ehlers MD. Modeling autism by SHANK gene mutations in mice. Neuron. 2013;78:8–27.
41. Monteiro P, Feng G. SHANK proteins: roles at the synapse and in autism spectrum disorder. Nat Rev Neurosci. 2017;18:147–57.
42. Naisbitt S, Kim E, Tu JC, Xiao B, Sala C, Valtschanoff J, et al. Shank, a novel family of postsynaptic density proteins that binds to the NMDA receptor/PSD-95/GKAP complex and cortactin. Neuron. 1999;23:569–82.
43. Peca J, Feliciano C, Ting JT, Wang W, Wells MF, Venkatraman TN, et al. Shank3 mutant mice display autistic-like behaviours and striatal dysfunction. Nature. 2011;472:437–42.
44. Zhu L, Wang X, Li XL, Towers A, Cao X, Wang P, et al. Epigenetic dysregulation of SHANK3 in brain tissues from individuals with autism spectrum disorders. Hum Mol Genet. 2014;23:1563–78.
45. Wang X, Xu Q, Bey AL, Lee Y, Jiang YH. Transcriptional and functional complexity of Shank3 provides a molecular framework to understand the phenotypic heterogeneity of SHANK3 causing autism and Shank3 mutant mice. Mol Autism. 2014;5:30.
46. Spence EF, Dube S, Uezu A, Locke M, Soderblom EJ, Soderling SH. In vivo proximity proteomics of nascent synapses reveals a novel regulator of cytoskeleton-mediated synaptic maturation. Nat Commun. 2019;10:386.
47. Soto JS, Jami-Alahmadi Y, Chacon J, Moye SL, Diaz-Castro B, Wohlschlegel JA, et al. Astrocyte-neuron subproteomes and obsessive-compulsive disorder mechanisms. Nature. 2023;616:764–73.
48. Mathew B, Bathla S, Williams KR, Nairn AC. Deciphering spatial protein-protein interactions in brain using proximity labeling. Mol Cell Proteomics. 2022;21:100422.
49. Branon TC, Bosch JA, Sanchez AD, Udeshi ND, Svinkina T, Carr SA, et al. Efficient proximity labeling in living cells and organisms with TurboID. Nat Biotechnol. 2018;36:880–7.
50. Song JH, Lucaci D, Calangiu I, Brown MTC, Park JS, Kim J, et al. Combining mGRASP and optogenetics enables high-resolution functional mapping of descending cortical projections. Cell Rep. 2018;24:1071–80.
51. Zhu F, Collins MO, Harmse J, Choudhary JS, Grant SGN, Komiyama NH. Cell-type-specific visualisation and biochemical isolation of endogenous synaptic proteins in mice. Eur J Neurosci. 2020;51:793–805.
52. Gupta I, Collier PG, Haase B, Mahfouz A, Joglekar A, Floyd T et al. Single-cell isoform RNA sequencing characterizes isoforms in thousands of cerebellar cells. Nat Biotechnol. 2018;36:1197–202.
53. Hardwick SA, Hu W, Joglekar A, Fan L, Collier PG, Foord C, et al. Single-nuclei isoform RNA sequencing unlocks barcoded exon connectivity in frozen brain tissue. Nat Biotechnol. 2022;40:1082–92.
54. Leblond CS, Nava C, Polge A, Gauthier J, Huguet G, Lumbroso S, et al. Meta-analysis of SHANK mutations in autism spectrum disorders: a gradient of severity in cognitive impairments. PLoS Genet. 2014;10:e1004580.
55. Kouser M, Speed HE, Dewey CM, Reimers JM, Widman AJ, Gupta N, et al. Loss of predominant Shank3 isoforms results in hippocampus-dependent impairments in behavior and synaptic transmission. J Neurosci. 2013;33:18448–68.
56. Wang W, Li C, Chen Q, van der Goes MS, Hawrot J, Yao AY, et al. Striatopallidal dysfunction underlies repetitive behavior in Shank3-deficient model of autism. J Clin Invest. 2017;127:1978–90.
57. Tao K, Chung M, Watarai A, Huang Z, Wang MY, Okuyama T. Disrupted social memory ensembles in the ventral hippocampus underlie social amnesia in autism-associated Shank3 mutant mice. Mol Psychiatry. 2022;27:2095–105.
58. Pagani M, Bertero A, Liska A, Galbusera A, Sabbioni M, Barsotti N, et al. Deletion of autism risk gene shank3 disrupts prefrontal connectivity. J Neurosci. 2019;39:5299–310.
59. Guo B, Chen J, Chen Q, Ren K, Feng D, Mao H, et al. Anterior cingulate cortex dysfunction underlies social deficits in Shank3 mutant mice. Nat Neurosci. 2019;22:1223–34.
60. Bhattacharya A, Vo DD, Jops C, Kim M, Wen C, Hervoso JL, et al. Isoform-level transcriptome-wide association uncovers genetic risk mechanisms for neuropsychiatric disorders in the human brain. Nat Genet. 2023;55:2117–28.
61. Gandal MJ, Zhang P, Hadjimichael E, Walker RL, Chen C, Liu S, et al. Transcriptome-wide isoform-level dysregulation in ASD, schizophrenia, and bipolar disorder. Science. 2018;362:eaat8127.
62. Benjamin KJM, Chen Q, Jaffe AE, Stolz JM, Collado-Torres L, Huuki-Myers LA, et al. Analysis of the caudate nucleus transcriptome in individuals with schizophrenia highlights effects of antipsychotics and new risk genes. Nat Neurosci. 2022;25:1559–68.
63. Araki Y, Hong I, Gamache TR, Ju S, Collado-Torres L, Shin JH, et al. SynGAP isoforms differentially regulate synaptic plasticity and dendritic development. Elife. 2020;9:e56273.
64. Johnson RC, Penzes P, Eipper BA, Mains RE. Isoforms of kalirin, a neuronal Dbl family member, generated through use of different 5′- and 3′-ends along with an internal translational initiation site. J Biol Chem. 2000;275:19324–33.
65. Sudhof TC. Synaptic neurexin complexes: a molecular code for the logic of neural circuits. Cell. 2017;171:745–69.

ACKNOWLEDGEMENTS

Imaging work was performed at the Northwestern University Center for Advanced Microscopy generously supported by NCI CCSG P30 CA060553 awarded to the Robert H Lurie Comprehensive Cancer Center. Y.Z.W was supported by the Brain & Behavior Research Foundation (2018 Young Investigator Grant, 27793). This research was also supported by an Individual Biomedical Research Award from The Hartwell Foundation and R01MH130428 to J.N.S. and a grant from CHDI foundation to D.J.S and J.N.S. We would like to thank Dr. Yong-Hui Jiang for kindly sharing us with the mouse Shank3A and 3E1 plasmids, Drs. Farida Vadimovna Korobova, Lennell Reynolds Jr and Wensheng Liu for their help with imaging, Dr. Jean-Francois Poulin's help in AAV injection, Kamil K Gebis' help on IHC experiments, Dr. Vahri Beaumont for image analysis, Dr. Sasha Ulrich for managing animals and Drs. Peter Penzes, Jones Griffith Parker and Savas lab members for proofreading this manuscript.

AUTHOR CONTRIBUTIONS

Y.Z.W, T.P.R, D.J.S and J.N.S designed the experiments. Y.Z.W, J.N.S, T.P.R and D.J.S wrote the manuscript. Y.Z.W, S.N.S. and T.P.R performed IHC and EM experiments. Y.Z.W performed all biochemical, dendritic spine morphological analysis and MS experiments. T.P.R performed all electrophysiological experiments and related data analysis. Y.Z.W performed the data analyses for IHC, EM, biochemical, dendritic spine morphological analysis and MS experiments.

COMPETING INTERESTS

The authors declare no competing interests.

ADDITIONAL INFORMATION

Supplementary information The online version contains supplementary material available at https://doi.org/10.1038/s41380-024-02493-w.

Correspondence and requests for materials should be addressed to Jeffrey N. Savas.

Reprints and permission information is available at http://www.nature.com/reprints

Publisher's note Springer Nature remains neutral with regard to jurisdictional claims in published maps and institutional affiliations.